Early subduction dynamics recorded by the metamorphic sole of the Mt. Albert ophiolitic complex (Gaspé, Quebec)

Benoît Dubacq, Mathieu Soret, Ella Jewison, Philippe Agard

▶ **To cite this version:**

Benoît Dubacq, Mathieu Soret, Ella Jewison, Philippe Agard. Early subduction dynamics recorded by the metamorphic sole of the Mt. Albert ophiolitic complex (Gaspé, Quebec). Lithos, 2019, 334-335, pp.161-179. 10.1016/j.lithos.2019.03.019 . hal-02187161

HAL Id: hal-02187161

https://hal.sorbonne-universite.fr/hal-02187161v1

Submitted on 17 Jul 2019

HAL is a multi-disciplinary open access archive for the deposit and dissemination of scientific research documents, whether they are published or not. The documents may come from teaching and research institutions in France or abroad, or from public or private research centers.

L'archive ouverte pluridisciplinaire **HAL**, est destinée au dépôt et à la diffusion de documents scientifiques de niveau recherche, publiés ou non, émanant des établissements d'enseignement et de recherche français ou étrangers, des laboratoires publics ou privés.

EARLY SUBDUCTION DYNAMICS RECORDED BY THE METAMORPHIC SOLE OF THE MT ALBERT OPHIOLITIC COMPLEX (GASPÉ, QUEBEC)

Benoît Dubacq[1,]*, Mathieu Soret[1,2], Ella Jewison[1], Philippe Agard[1]

1 Sorbonne Université, CNRS-INSU, Institut des Sciences de la Terre de Paris, ISTeP UMR 7193, F-875005 Paris, France

2 University of British Columbia, Okanagan, Earth, Environmental and Geographic Sciences Kelowna, BC, Canada

* corresponding author: Benoit.Dubacq@sorbonne-universite.fr

Keywords: metamorphic sole; subduction initiation; thermobarometry; Mont Albert; metamorphic petrology

1. INTRODUCTION

Understanding the mechanisms of emplacement of ophiolites has been the subject of decades of studies focused on the sole of these ophiolites (Williams and Smith, 1973; Searle and Malpas, 1982; Spray et al., 1984; Jamieson, 1986; Hacker, 1991; Mahmood et al., 1995; Gnos, 1998; Dimo-Lahitte et al., 2001; Ishikawa et al., 2005; Cowan et al., 2014; Rioux et al., 2016; amongst many others). Ophiolite soles are generally thin (<500 m) portions of heavily deformed peridotite and metamorphosed oceanic crust, found at the base of most large-scale ophiolites. Their present-day structure results from the stacking of three main units: one of mantle origin and two of crustal origin. Figure 1 presents a conceptualised frame for the formation of ophiolite soles during subduction infancy. The top of the sole, found beneath porphyroclastic peridotite, is typified by tectonized harzburgite with a mylonitic to ultramylonitic overprint, common occurrence of secondary clinopyroxene, amphibole and late serpentine. The median and lower units of the sole are metamorphic rocks of mainly mafic nature, with metamorphic grade decreasing downwards. These two units are commonly referred to as ‘metamorphic sole’, and originate from oceanic crust. They are interpreted as sea-floor mafics and sediments re-crystallising at depth, immediately below the nascent mantle wedge, within the first few million years of the life of the subduction/obduction system (e.g., Dewey, 1976; Wakabayashi and Dilek, 2000, 2003): the top of the subducted oceanic plate is metamorphosed up to granulite facies against the still hot overlying peridotite, and accreted to the base of the future ophiolite when the rheological contrast between the two is minimum (Agard et al., 2016 and Fig. 1 a-b). This allows exhumation of the sole together with the ophiolitic body, as subduction proceeds until obduction (Fig. 1c). The consistency of ductile strain in the high-grade metamorphic rocks of the sole and in the deformed peridotite (top of the sole) has led numerous authors to suggest these units share common history (e.g. Searle & Malpas, 1980; Boudier et al., 1982; Spray, 1984; Jamieson, 1986; Prigent et al., 2018), including exhumation. In this model, burial of the oceanic crust and exhumation of the sole are fast, which is supported by dating (e.g., Hacker and Mosenfelder, 1996; Hacker et al., 1996). Later blueschist facies metamorphism is observed in margin units originating further away from the trench (as for the Saih Hatat region in Oman, e.g. Agard et al., 2010)

and less frequently in the metamorphic sole itself (Wakabayashi, 1990; Plunder et al., 2016), an evidence of cooling of the geothermal gradient over time. In this general scheme, the metamorphic rocks originating from subducted oceanic crust contain essential information about ophiolite emplacement and geological processes occurring at the plate interface in nascent subduction zones. In the overlying peridotite, information is lacking or much less precise in terms of evaluating strain mechanisms, estimating geothermal gradients (through thermobarometry) and dating (with e.g. U-Pb radiochronology on granitoid rocks from slab melting, $^{40}Ar/^{39}Ar$ on amphibole). Chemical exchange from crust-derived metamorphic rocks to peridotites at the base of ophiolitic massifs has also been documented as a proxy to mantle wedge metasomatism and linked to dehydration reactions in metamorphic soles together with deformation and refertilisation of the peridotite (e.g. Ishikawa et al., 2005; Linckens et al., 2011; Soret et al., 2016; Prigent et al., 2018).

Continued petrological and structural work, largely based on the Cenomanian Semail ophiolite (in Oman and United Arab Emirates) but also carried out on much older ophiolites such as found in the Ordovician Bay of Islands complex (see compilation in Agard et al., 2016), has revealed impressive consistency in the peak metamorphic conditions of metamorphic soles, with an apparent inverted metamorphic gradient. The high-temperature unit at the top of the metamorphic sole is metamorphosed and accreted first, around 1 GPa and 850°C, then the lower unit is accreted around 0.5 GPa and 550°C. Soret et al. (2017) have shown that this process has been acting repetitively for step-wise accretion of subunits within the high-temperature unit of the Semail ophiolite. Interestingly, and in line with the consistency of pressure-temperature estimates between and within metamorphic soles, no evidence has been found for a link with the paleo-location of the ridge crest of the structurally overlying ophiolitic units: in Oman, metamorphic sole is found on both sides of the paleo-ridge, with identical conditions of crystallisation.

Despite progress on thermodynamic models for amphibole and mafic systems (see Green et al., 2016; Palin et al., 2016), large uncertainties remain on the depth of accretion and on pressure-temperature-time paths of metamorphic soles due to their chiefly mafic nature (making thermobarometry imprecise compared to metapelites). In the present context of subduction initiation, a counter-clockwise pressure-temperature path is expected following general cooling of the geothermal gradient through

time, as presented by Hacker and Gnos (1997) or Searle and Cox (1999) for the Semail ophiolite. However thermo-mechanical modelling of obduction of this ophiolite (Duretz et al., 2016) yielded clockwise pressure-temperature paths for units equivalent to metamorphic soles, with a clockwise component increasing away from the plate interface. Yet no clockwise or counter-clockwise component was evidenced by Soret et al. (2017) due to limited preservation of the prograde history.

In this publication, a petrological study of selected sections through the sole of the Mont Albert ophiolitic complex (Quebec, Canada) is reported. Although exposure quality is poor due to forest cover, the crustal section of the sole appears generally fresh with limited greenschist-facies retrogression. The petrology of the sole is similar to that of the Semail ophiolite, with the advantage that thin layers of aluminosilicate-bearing metapelites are found scattered within subunits of the Mont Albert sole, partly preserving prograde mineral assemblages. The diversity of mineral assemblages in metapelites allows deriving robust estimates of the peak metamorphic conditions, consistently with thermodynamic modelling of the metamorphism of the mafic rocks. As for the Semail ophiolite, units and subunits in the metamorphic sole of the Mont Albert ophiolitic complex appear accreted in a step-wise manner. Estimated pressure-temperature paths are clockwise, with exhumation above the plate interface along a warmer thermal gradient than burial. This has implications for the evolution of the thermal gradient around the plate interface. Clockwise pressure-temperature paths are reconciled with the progressive cooling of the plate interface by rapid accretion and exhumation of metamorphic soles, within the first few million years of subduction initiation.

2. GEOLOGICAL SETTING

2.1. Structural organization and radiometric constraints

The Mont Albert ophiolitic complex (Fig. 2) is located 35 km south-east of the shore of the Saint Lawrence river and the city of Sainte-Anne-des-Monts, in the Gaspé Peninsula of the Quebec province of Canada. The Mont Albert ophiolitic complex is an incomplete Ordovician ophiolitic sequence (Beaudin, 1983; Gueddari et al., 1999) with peridotite overlying a metamorphic sole mainly composed of amphibolite (‘*amphibolite du diable’*) showing an apparent inverted metamorphic gradient. A few kilometres to the south-west, Mont Paul and Mont du Sud are part of the same ophiolitic system and are included in the Mont Albert ophiolitic complex. There is no remnant of crustal rocks above the

peridotite, therefore the age of the ophiolitic complex has been constrained in earlier studies with radiometric dating carried out on the metamorphic sole and with structural and stratigraphic correlation.

The Mont Albert peridotite and its basal amphibolite are classified in the Dunnage zone and correlated to a series of Quebec ophiolites (including from south to north: the Mount Orford, Lac Brompton, Asbestos, Thetford Mines ophiolites) via a Taconian suture zone between Laurentia and Lower Palaeozoic peri-Laurentian terranes (see Pinet and Tremblay, 1995; Malo et al., 2001, 2008; De Souza et al., 2012; Tremblay and Pinet, 2016). This suture zone extends along the Appalachians to western Newfoundland, where the Bay of Islands Complex, a klippe of the Dunnage zone, is the most complete ophiolite of the orogeny (Cawood and Suhr, 1992). The Dunnage zone represents the Ordovician oceanic basin related to the Iapetus ocean and located outboard of the continental passive margin of Laurentia defining the Humber zone (Williams, 1979; De Souza et al., 2014). The Mont Albert ophiolite and its sole overlay unconformably the Schick-Schock volcanic flows and pyroclastics metamorphosed to lower greenschist facies that appear in the internal Humber zone in recent publications (reviewed in Tremblay and Pinet, 2016), although Lux (1986) suggested they are part of the Dunnage zone. These volcanics are subalkaline tholeiitic basalts of N-MORB-type, with geochemical evidence in favour of their eruption in the Humber Zone during the rifting event which led to the opening of the Iapetus ocean (Camiré et al., 1995). The Mont Albert ophiolitic complex is separated from the upper Ordovician to Devonian sediments and volcanics of the Gaspé Belt to the south by a fault zone (Schick-Schock South Fault, Fig. 2) part of the Baie Verte-Brompton Line.

Radiometric dating using $^{40}Ar/^{39}Ar$ by Malo et al. (2008) on amphibole yielded cooling ages in the range 457-461 Ma for the highest-grade metamorphic rocks of the sole, crystallisation ages in the ranges 454-458 Ma for the lower grade metamorphics of the sole and 455-456 Ma for the greenschist facies overprint of the Schick-Schock Group, in agreement with earlier ages (Lux, 1986; Pincivy et al., 2003). These ages are in the same range as the 456 (+/-5) Ma U/Pb age obtained among older ages by Trzcienski et al. (1995, unreviewed) on zircon from an “unusual magnetite-rich orthopyroxenite layer” in the peridotite, as reported by Pincivy et al. (2003) and Tremblay and Pinet (2016).

2.2. Nature of the ophiolitic complex

The Mont Albert ophiolitic complex has first been mapped in detail by Alcock (1927) who interpreted it as a lenticular magmatic injection, where the surrounding amphibolite was thought representative of early magmatic phases, followed by the principal ultramafic body. MacGregor and Basu (1979) present a detailed petrographic review of the Mont Albert massif based on extensive sampling and electron microprobe analyses carried out in the mid to late 1960s. These authors regard the massif as an ultramafic intrusion into the Schick-Schock group, the amphibolite being interpreted as a contact metamorphism aureole into which they identified kyanite-bearing gneisses and possible partial melting (see also MacGregor, 1964).

The ophiolitic nature *sensu stricto* of the Mont Albert massif has been popularised by the study of Beaudin (1983). Trzcienski (1988) later suggested that its metamorphic sole was a retrogressed eclogite, using the co-existence of garnet and clinopyroxene in the high-temperature unit for the terminology but suggesting peak metamorphism around 840°C and at least 1.2 GPa to account for the presence of kyanite in metasediments – which corresponds to the upper garnet granulite field as defined by Spear (1993). In this view, the whole metamorphic sole and peridotite massif were subducted and later exhumed along the surrounding faults in the stability field of kyanite (buried along a thermal gradient around 16°C/km). Rejecting the eclogitic nature of the sole in line with other authors (e.g. O'Beirne-Ryan et al., 1990), Whitehead et al. (1995) interpreted the *amphibolite du diable* as a dynamothermal sole formed ‘in a shear zone within an oceanic domain by the progressive underplating of overridden crustal rocks to the base of an overriding oceanic fragment’, where shear heating implicitly plays a prominent role as heat source. This definition is not necessarily inconsistent with current models (e.g. Agard et al., 2016; Rioux et al., 2016) but overlooks the apparent pressure gradient and the depth of the process as implied by kyanite, which eases explaining dating inconsistencies between initiation of basin closure based on fossil evidence and $^{40}Ar/^{39}Ar$ cooling ages on the amphibolite appearing 20 Ma older (Whitehead et al., 1995).

There is now little doubt on the ophiolitic nature of the Mont Albert (and associated Mont Paul and Mont Du Sud), mostly thanks to large-scale studies of ophiolites obducted during the Taconian

orogeny showing clear consistency both in terms of petrography and ages along the north-eastern Appalachians (e.g. Whitehead et al., 1995; Pincivy et al., 2003; Malo et al., 2008; De Souza et al., 2012; Tremblay and Pinet, 2016). Tremblay and Pinet (2016, and references therein) advocate genesis of these ophiolites within a supra-subduction zone environment – with already-established plate convergence – based on extensive evidence of subduction of the Laurentian margin prior and during ophiolite formation. Similarly, the metamorphic sole is now interpreted as formed in a process equivalent to that of the Semail ophiolite and other soles worldwide, as discussed at length by Agard et al. (2016).

3. NATURE, STRUCTURE AND DEFORMATION OF THE SOLE

The Mont Albert, Mont Paul and Mont du Sud are characterised by alpine tundra and rare krummholz on the peridotite (studied by e.g. Sirois and Grandtner, 1992; Martin and Germain, 2016) contrasting with the generally dense forest cover found over most of the *amphibolite du diable*. Exposure of the metamorphic sole is further restrained by the presence of numerous boulders of both local and remote origin related to the last glacial maximum (see Olejczyk and Gray, 2007). Consequently, exposed sections through the metamorphic sole are not continuous over scales of hundreds of metres as in Oman, complicating the study of mineralogical changes with distance to the contact of the peridotite, as folding and possible late faulting cannot be rigorously evaluated. The Mont Albert ophiolitic complex has nevertheless been mapped in detail and shows a simple structure, with the peridotite monotonously overlying the metamorphic sole, and mappable metamorphic grades within the sole (Fig. 2b-c).

The overall structure of the Mont Albert is a large syncline with fold axis around 240° (e.g. MacGregor and Basu, 1979; Gagnon and Jamieson, 1986). Exposure of the sole is best on the northern part of the massif, where foliation is parallel to the contact and dips steeply to the south in the range 50-70°. In order to show a representative section through the metamorphic sole of the Mont Albert ophiolitic complex, a schematic log based on several small-scale sections is provided in figure 3a with field photographs (Fig. 3b-l). Late small-scale normal faulting on the north-east ridge of the massif, related to the ‘*Marches du Géant’* fault system (Malo et al., 2008), only allows for approximate evaluation of the structural distance of metamorphic sole outcrops to the contact with the peridotite.

The following general description starts from the structural summit of the ophiolitic complex, going downwards, with distances expressed as the apparent structural distance to the contact.

3.1. Structure and mineralogy of the peridotite

The peridotite is typified by harzburgite with earth yellow to brass colour due to weathering (Fig. 3b-c-d-e). 49 samples have been collected and studied for their mineralogy, which will be detailed elsewhere.

Serpentinisation is pervasive, altering the rock density on various degrees. The base of the peridotite is mapped as a ~20 m-thick serpentinite layer (Fig. 3 d) where serpentinisation is generally intense and accompanied by minor chalcedony. This serpentinite layer is not regarded as representative of the entire part of the sole with peridotite origin (part of red rectangle in the mantle wedge in Fig. 1c) first because contacts between this layer and the less serpentinised peridotite are only clear on the north-eastern part of the massif, then due to the fact that porphyroclastic peridotite is dominant hundreds of metres away from the contact, as observed by MacGregor (1979, using whole texture and chromian spinel as a strain indicator insensitive to serpentinisation). Therefore the extent of the deformed peridotite section of the sole into the mantle sequence is unclear. Away from this serpentinite layer, serpentinisation remains important irrespective of the distance from the contact with the amphibolite metamorphic sole. Grain size varies wildly from cm-scale orthopyroxene forming positive relief alteration to micrometric crystals in peridotite with ultramylonitic texture (see also Laurent and Hebert, 1979; MacGregor, 1979). Dunite and minor amphibole-bearing lherzolite and websterite are found inter-layered with the harzburgite. In thin section, amphibole (consisting of pargasite, Mg-hornblende and tremolite) appears of metamorphic origin linked to deformation stages in mylonites, together with secondary olivine, aluminous spinel and clinopyroxene. Metre-thick chromitite lenses with aspect ratio around 10 are sporadically found along the axial plane of the syncline with associated kammererite (mauvish pink Cr-Mg-chlorite, as reported by MacGregor and Basu, 1979). Penninite (Mg-chlorite with Si content greater than that of clinochlore) is frequently found all over the massif in haloes around chromian spinel. The main foliation in the peridotite is highlighted by serpentine-rich planes and clearly parallel to the contact with the metamorphic sole when observed on the northern

part of the massif (Fig. 3e, also Gagnon and Jamieson, 1986). Outcrops on the south-west part of the massif (near lake Isabelle) are obscured by intense serpentinisation and provide only poor exposure of the base of the peridotite.

3.2. Metamorphic rocks from the sole

The high-grade unit of the *amphibolite du diable* is found underlying the peridotite (Fig. 3b-e-f-g). It is a heterogeneous but generally massive, dark, mafic metamorphic rock with well-defined foliation but without clear evidence for simple shear deformation. Lineation was only found for late amphibole. The maximum thickness of this unit is estimated in the range 80-100 m. Metamorphic grade decreases away from the contact. The term amphibolite to describe rocks immediately below the contact is somewhat abusive as amphibole content may be as low as 30%, with more abundant garnet-clinopyroxene assemblage in varying relative amounts and minor plagioclase (1-5%). Orthopyroxene was not observed. Grains are generally millimetre-sized (1-5 mm) with garnet occasionally reaching 1 cm. Away from the contact, the amphibole and plagioclase content increases (apparently gradually) at the expense of garnet and clinopyroxene, which disappear from mafic rocks about 15 m (for garnet) and 25 m (for clinopyroxene) away from the contact. Garnet amphibolite is also found ~250 m from the contact on the north-eastern flank of Mont Olivine, in rocks that are apparently large (>10 m) boulders with no connection to the bedrock. Grain size decreases away from the contact to approximate 0.5 mm in the garnet-absent amphibolite. Epidote is ubiquitous as a retrogression phase, rimming clinopyroxene and amphibole, and as individual crystals, in varying amounts (<1 to 10%). Garnet-rich layers (Fig. 3g) and iron oxide-rich layers are found alternating with the garnet-clinopyroxene mafic rocks close to the contact. The iron oxide-rich layers contain abundant chlorite, mica and epidote. Corundum is observed in some of these layers <10 m away from the contact.

About 35 m away from the contact, an intriguing pinkish 1.5 m-thick quartz-plagioclase-amphibole-biotite-sphene-garnet layer with retrogressed pegmatitic texture is found cutting the foliation at a low angle (Fig. 3h). Of seemingly magmatic origin, it probably corresponds to the outcrop described and interpreted by Gagnon and Jamieson (1986) as a dyke injected after the metamorphic sole developed its foliation. Due to its orientation with respect to the foliation, we prefer referring to this as a sill. It is

heavily retrogressed with epidote on its margins co-existing with white and dark mica, and fibro-radial gedrite.

Rare biotite-rich layers are found within 20 m from the contact. The first clear occurrences of aluminous metapelites appear about 25 m away from the contact as alternating dark red and pale grey layers ranging between 2 and 20 cm in thickness within the mafic rocks (metapelites are more easily identified in fallen boulders on the flanks of the north-east arête of the Mont Albert and on the north path to the summit just before the final ascent). These metapelites contain biotite (in greater proportions in the dark red layers), quartz, plagioclase, garnet, sillimanite, staurolite and muscovite as described below in greater detail, with scapolite, Fe-Ti oxides, epidote and chlorite in varying but generally minor proportions. Further away from the contact (45-55 m, Fig. 3i), pelitic schists contain kyanite with abundant mm-sized garnet, biotite, quartz, plagioclase, epidote and late muscovite.

The low-grade unit of the metamorphic sole (Fig. 3j-l) is typified by metabasalt with “inverted” metamorphic grade within the upper greenschist to amphibolite facies. A section with good exposure is found on the shore of the Cascapedia river towards Mont du Sud; other interesting outcrops include the shore of the lake on top of ‘*ruisseau du Plaque Malade*’, the base of the north-east arête of Mont Albert (corresponding to the fourth zone described by Gagnon and Jamieson, 1986) and the path south of *Lac du Diable* (where O'Beirne-Ryan et al., 1990, reported sporadic migmatites, which were not confidently identified in this study). The difference between the base of the high-grade unit and the top of the low-grade unit is not clear-cut in terms of metamorphic grade. However these units differ in terms of strain and retrogression. The lower unit is variably spilitized (see e.g. Skelton et al., 2010 for comparison) and shows shearing and boudinage of former pillow-lavas (Fig 3j-k) together with ubiquitous recumbent folding highlighted by feldspar-rich layers (felsic amphibolite of Gagnon and Jamieson, 1986). In addition to green amphibole, albite, epidote and chlorite are present. The top of the unit is rich in iron oxide, the base contains pyrite up to ~2 mm-large.

Metasediments in the low-grade unit appear mainly as quartzite, in proportion of 5-10 % of the sole thickness. White mica, chlorite and rare garnet have been found disseminated in the quartzite and in cm-thick beds.

264

265

Rock type	Main unit	Main minerals (>5%)	Minor minerals (≤5%)	Accidental minerals (<1%)
amphibolite	high grade	Amp, Pl, Cpx	Grt, Opq, Ep, Rt	Ser, alt. φ
metasomatic rocks	high grade	Ep, Chl, Opq	Crn, Mrg, Pg, Rt	Qz, Ms, Spn
amphibolite	low grade	Amp, Qz, Ep, Chl	Cal, Fsp	Opq, Ccp
quartzite	low grade	Qz, Pl, Bt, Ep	Chl	
amphibolite	low grade	Amp, Qz, Ep, Pl	Opq	
amphibolite	low grade	Amp, Ep, Pl, Opq	Qz	Cc, Spn
amphibolite	low grade	Amp, Pl, Ep, Chl	Qz, Opq	Cc
amphibolite	low grade	Amp, Ep, Opq	Qz	Cc, Spn
schistose layer in quartzite	low grade	Amp, Qz, Pl, Ep, Chl	Opq	Spn
schistose layer in quartzite	low grade	Phg, Qz, Opq, Chl, Amp	Grt, Ep	Cc
amphibolite	low grade	Amp, Ep, Pl, Qz	Opq	
amphibolite	low grade	Amp, Ep, Qz	Pl, Cc, Opq	
amphibolite	high grade	Amp, Cpx, Ep, Opq	Pl	Fsp
amphibolite	high grade	Grt, Amp, Cpx, Ep	Pl, alt. φ	Ccp, Cv
amphibolite	high grade	Amp, Cpx, Ep, Opq	alt. φ	
amphibolite	high grade	Cpx, Grt, Amp, Ep	Pl, alt. φ	Qz

amphibolite with garnet layer	high grade	Grt, Amp, Cpx, Ep		
amphibolite	high grade	Amp, Cpx, Pl, Ep	alt. φ	Mrg
amphibolite	intermediate	Amp, Cpx, Pl, Ep, Mrg	Ser, alt. φ	Ccp, Cv
Sill / metasediment contact	high grade	Fsp, Qz, Chl, Amp	Ms, Bt, Grt, Opq	Ep, Aln, Spn
metapelite	high grade	Ab, Qz, Chl, Ep, Grt, Opq	Ms, Ap, Bt	Mnz
metapelite	high grade	Qz, Grt, Phg, Bt	St, Opq, Ky, Pl	Rt, Chl
metapelite	high grade	Qz, Ms, Bt, Grt, Pl, Ky	Opq, Ep	Chl
sill	high grade	Ab, Amp, Spn, Opq	Ep, Ms	Mnz
metapelite	high grade	Bt, Qz, Ep, Grt	Pl, Opq	Chl, Zrn
metapelite	high grade	Qz, Pl, Grt, Phg	Bt, Spn, Ep	Rt, Chl
metapelite	high grade	Phg, Grt, Qz, Pl	Bt, Spn, Ky	Amp, Chl, Ap
metapelite	high grade	Grt, Bt, Pl, Sil, Opq	St, Phg, Scp	

266Table 1. Mineralogy of samples used in this article. Main minerals are sorted from more to less abundant. Alt. φ: minute alteration phases replacing plagio-

267clase (Ms, Mrg, Ntr, Ep etc., see Fig. 4).

4. PETROGRAPHY AND MINERALOGY

In this section, the textural relationships between minerals are presented with microphotographs and SEM images, separating metabasalts from rocks with sedimentary protoliths. The 'sill' (Fig. 3h) and oxide-rich layers are presented with the non-mafic metamorphic rocks. The mineralogy is summarized in table 1. All abbreviations in figures, tables and appendix are after Whitney and Evans (2010).

4.1. Sampling and analytical techniques

104 samples have been collected on the Mont Albert and Mont du Sud massifs. Only samples from the metamorphic sole are presented here (using 29 samples selected out of the 55 metamorphic rocks collected). Scanning electron microscopy (SEM) was used after optical microscopy at ISTeP (Sorbonne Université, Paris, France) using a Zeiss Supra 55VP apparatus associated to a SSD detector PTG Sahara for imaging and elemental mapping in energy-dispersive spectroscopy mode.

Electron probe micro-analyses were carried out at CAMPARIS (Sorbonne Université, Paris, France) with both Cameca SX-5 and SX-100 instruments. Point measurements were made in classical analytical conditions (15 kV acceleration voltage and 10 nA beam current allowing ~2µm beam size in wavelength-dispersive spectroscopy mode) using diopside (Ca, Mg, Si), $MnTiO_3$ (Mn, Ti), orthoclase (K, Al), Fe_2O_3 (Fe), albite (Na) and Cr_2O_3 (Cr) as standards for calibration of elements indicated in parentheses. Elemental mapping has been carried out with identical voltage and either 10 nA current and counting time of 300 ms per point or with increased current (100 nA) and counting time of 100 ms per point. Analyses were calibrated with the manufacturer's software using standards as for point analyses, and it was ensured that results of mapping were consistent with point measurements.

4.2. Mafic rocks

4.2.1.High grade unit

At the thin-section scale, rocks sampled at the contact with the peridotite show porphyroblastic texture (Fig. 4a) with garnet, pale green clinopyroxene, deep green amphibole crystals aligned within the foliation, plagioclase and epidote. Garnet is typically millimetre-sized and disseminated throughout samples (Fig. 4b) or in garnet-rich layers (Fig. 3g). Quartz inclusions are rarely (~5%) found in garnet porphyroblasts. Clinopyroxene appears as large (>5 mm) crystals with undulose extinction, and in

small (100-500 μm) optically homogeneous crystals. Clinopyroxene is found disseminated in the rock and in cm-thick bands (Fig. 4b) parallel to the amphibole foliation and showing both types of crystals. Several types of symplectite are found throughout the samples, involving garnet, clinopyroxene, amphibole, plagioclase, oxides and epidote, with all six phases or a combination of some of them. Clinopyroxene-amphibole symplectite with and without plagioclase (Fig. 4f) is observed wherever clinopyroxene is stable. Epidote-amphibole symplectite is seen in some rocks less than 10 m away from the contact. Garnet-clinopyroxene symplectite with plagioclase or with epidote and oxides (Fig. 4f and g), both usually with retrogressive mica, are found in garnet-bearing samples regardless of the distance to the contact. Plagioclase in the symplectite is rarely preserved. It is usually replaced by fine intergrowths of epidote and muscovite (Fig. 4 h-i). Under the optical microscope, these intergrowths appear as a dark, turbid phase (Fig. 4d-e-g) with second order birefringence tentatively identified as diaspore by O'Beirne-Ryan et al. (1990). In this study diaspore has not been found in these intergrowths, instead margarite, albite, adularia and natrolite appear as frequent alteration products of the (previously-retrogressed?) plagioclase (Fig. 4 h-i). Chalcopyrite is found sporadically throughout retrogression assemblages, accidentally with covellite. Translucent epidote crystals are frequently associated with retrogressed plagioclase, and late yellow epidote cross-cuts most samples, chiefly along the foliation and less frequently at a sharp angle with it. This leads to compositional banding on the scale of centimetres in some samples, as noted by O'Beirne-Ryan et al. (1990). In the clinopyroxene-free zone, pale yellow epidote is aligned with the amphibole (Fig. 4h) and makes up to 40% of the sample. Large amphibole crystals are often zoned, with pale green cores and darker rims (Fig. 4a).

4.2.2.Low grade unit

Strain is marked by folding in the low-grade part of the metamorphic sole. The top of this unit is characterized by elongated, ~100 μm-long amphibole showing a well-marked foliation, sometimes with crenulation (Fig. 5b). However crystal size may be larger with amphibole reaching 3 mm in some samples. Albite is ubiquitous and makes up to 50% of some samples. Sphene, chlorite, hematite and ilmenite are observed in almost all samples. Orthoclase has been found in samples on the south end of the section along the Cascapedia river. Calcite-filled spherulites with epidote rims (Fig. 5c) are

interpreted as former vesicles (see e.g. Schiffman and Staudigel, 1995). These are increasingly found downwards in the metamorphic sole and show evidence of shearing. Amphibole is more heterogeneous downwards, with pale green cores and darker blue-green rims (Fig. 5a). Symplectites are not observed.

4.3. Metasediments and non-mafic rocks

Sillimanite-bearing metapelites (closest to the contact, Fig. 6f-g-h) have well-developed schistosity marked by biotite. Euhedral to sub-euhedral mm-sized garnet is found co-existing with prismatic sillimanite and well-preserved plagioclase including sillimanite needles (Fig. 6f). Garnet hosts numerous inclusions: biotite (~300 µm), oxides, staurolite, plagioclase, apatite, sillimanite (Fig. 6h) and abundant negative crystal shape inclusions resembling peritectic silicate melt inclusions found in migmatites and granulites (nanogranites, see Fig. 6h-i and Cesare et al., 2015). Titano-ilmenite is found in infrequent but large (cm-sized) crystals around garnet and plagioclase, it shows generalized exsolution. Scapolite appears in large (~1cm) poikilitic crystals. Staurolite is found both in the foliation and cutting the foliation, including titano-ilmenite and plagioclase (Fig. 6f-g). Staurolite in contact with plagioclase and sillimanite is often euhedral with some faces resorbed. The staurolite at an angle with the foliation is locally observed growing on garnet. Muscovite is present as a late phase at sharp angle with the foliation.

Red oxide-rich layers apparently associated with metasediments in the field contain corundum, epidote and abundant Fe-Ti oxides (Fig. 6d-e). Corundum appears dark blue in thin section due to numerous minute rutile inclusions. It is haloed by margarite, paragonite and diaspore, associated with chlorite, all cross-cutting the foliation marked by epidote and corundum. These assemblages and their retrogression have already been mentioned in gneissic metabasalts in contact with peridotite (Bucher et al., 2005 ; Operta et al., 2003; Pratt, 1906) and interpreted as the product of fluid-rock interactions and metasomatism of metasediments in contact with ultramafic rocks.

Minerals in the ‘sill’ 35 m away from the contact (§ 3.3; Fig. 3h) are strongly retrogressed (Fig. 6d), with little textural evidence preserved. The apparent foliation is defined by amphibole and biotite. Some amphibole crystals are also oriented within shear bands filled with euhedral iron oxide. Quartz shows undulose extinction. Plagioclase is sericitised. Epidote veins cross-cut the sample. Biotite is

mostly replaced by chlorite, and muscovite grains are again oriented perpendicular to the foliation. Garnet crystals are more abundant on the margins and contain quartz and Fe-Ti-oxides inclusions. Neither kyanite nor sillimanite was observed.

Kyanite-bearing schists shown in figures 3i and 6a-c, sampled ~50 m away from the contact, contain 5 mm-large garnet, quartz, biotite, plagioclase, muscovite, apatite, rutile, epidote and late chlorite growing after biotite. Sillimanite, fibrolite and nanogranite-like inclusions have not been confidently identified in these samples. Staurolite is only found included in garnet (Fig. 6c), together with muscovite, apatite and biotite. Accidental 30 µm monazite has been found.

In the deformed low-grade unit of the metamorphic sole, chlorite-mica-bearing quartzites show a well-developed foliation with oriented phyllosilicates. Crenulation cleavage is observed in all samples. Garnet is rare (5%, in one sample) and includes apatite and chlorite. Albite is found disseminated in thin sections, with calcite and epidote. Muscovite and chlorite are intergrown, with minor biotite. These are generally smaller than 20 µm.

5. MINERAL COMPOSITION

Representative electron probe micro-analyses are provided in tables in appendix for amphibole (A1), clinopyroxene (A2), plagioclase (A3), micas (A4), epidote (A5), garnet (A6) and accessory phases (A7, including staurolite, chlorite, margarite, scapolite and pumpellyite).

5.1. Mafic rocks

Garnet in high-grade mafic rocks is a solid solution with 40-60% almandine, 12-30% pyrope, 18-45% grossular and minor spessartine content (≤7%). Garnet zoning is bimodal, with homogeneous cores and spessartine - almandine-rich rims, best seen on the Mn map content (Fig. 7a-c). Mn-enriched zones correspond to the garnet rim with symplectic texture, crystallising with plagioclase and clinopyroxene. It is noteworthy that symplectic garnet is found surrounding homogeneous Mn-poor garnet. Mn enrichment is systematic around garnet cores and followed by Mn depletion in largest symplectites (Fig. 7c). The systematic pattern implies that garnet rims with symplectite texture were produced, not consumed, during symplectite growth, in contrast with kelyphite usually associated to garnet consumption during retrogressive decompression (Messiga and Bettini, 1990). In this view, Mn depletion is a reservoir effect during symplectite growth (as for classical Mn bell-shaped zoning in

380garnet) not necessarily related to changing pressure-temperature conditions (e.g. Kohn, 2003; Tropper
381and Recheis, 2003).
382Clinopyroxene (Fig. 7c-d-e) is of diopside type with X_{Mg} (defined as $Mg/(Mg+Fe^{2+})$ pfu) in the range
3830.6-0.8, Na content between 0.04 and 0.06 apfu, and Al content between 0.10 and 0.35 apfu. Samples
384closest to the contact have varying X_{Mg} (from 0.60 to 0.75) and highest jadeite content (sample MA-
38514-35, ~2 metres off the contact). Further away from the contact, large clinopyroxene crystals within
386the foliation have lowest Al. Al is high in small pyroxene crystals and in crystal cores, and low in the
387pyroxene with symplectite texture (Fig. 7b and 8d). X_{Mg} increases with decreasing Al content.
388Figure 9 shows the compositional variation of amphibole in high and low-grade mafic units.
389Amphibole close to the contact shows compositional zoning between ferroan pargasite and
390tschermakitic hornblende (both sampled 5-8 m away of the contact) using the definition and site
391repartition of Leake et al. (1997). Corresponding Ti content reaches 0.20 apfu for the pargasite and
392decreases steadily with increasing Si content towards Ti-free actinolite. Amphibole in the low-grade
393unit is often zoned, with Al-poor cores and Al-rich rims (corresponding to Si-rich, Ti-poor cores and
394Si ~6.5, Ti~0.05 apfu rims, see Fig. 9a-b-c), consistently with colour variations marked by paler cores.
395Feldspars mainly consist of plagioclase, orthoclase (or adularia) and albite (Fig. 9d). Extensive
396retrogression of plagioclase in the garnet-clinopyroxene symplectite complicates EPMA
397measurements and prevents studying zoning. Anorthite content in plagioclase ranges between 75 and
39892% in the high-grade section with garnet and clinopyroxene. Further away from the contact and in
399the low-grade section, plagioclase is of oligoclase type with anorthite content in the range 17-30%.
400Albite, orthoclase and adularia are found in samples from the low-grade unit and unequivocally
401associated to retrogression. Interstitial sanidine with complex twinning around ~40% orthoclase (Fig.
4029d) was accidentally found in samples where plagioclase content is low (<5%, samples MA-14-22 and
403MA-14-34).
404Epidote (Fig. 10) is a solid solution varying from a clinozoisite-rich component (maximum Al content
405= 2.87 apfu found in our samples) to a pistacite-rich component (Fe^{3+} = 1 apfu). The more aluminous
406compositions are restricted to the high-grade section of the metamorphic sole, and ferric epidote is
407observed in almost all mafic samples regardless of metamorphic grade, as individual crystals,

overgrowths and in veinlets cross-cutting the foliation (Fig. 10b-c). In high-grade rocks, Al-rich epidote is observed associated to retrogressed plagioclase (Fig. 7d), corundum-rich layers and with the garnet-clinopyroxene-amphibole symplectite. Allanite is sporadically found in low-grade mafics with ferric epidote overgrowths.

Chlorite is of chamosite type (mostly tri-trioctahedral with octahedral sum greater than 5.90) and has X_{Mg} between 0.55 and 0.70, with highest values reached in corundum-epidote-bearing samples close to the contact and lowest X_{Mg} in the low-grade section of the sole. Only sample MA-14-22 shows zoning, with crystal cores at Si = 3.0 apfu and edges/rims at Si = 2.7 apfu. Other samples have Si content in the range 2.55-2.74 with little variations within sample.

5.2. Metasediments and "intrusion"

Figure 11 presents mineral compositions for garnet, biotite, feldspar and phengite for the metapelites and metacherts found in the metamorphic sole of Mont Albert.

Garnet in metapelites from the high-grade section is a solid solution between almandine (55-80%), grossular (5-25%), pyrope (10-25%) and minor spessartine component (<7%). Zoning is ubiquitous with concentric, oscillatory and fracture-sealing zoning best observed in Mn and Ca (Fig. 11 b,c). Ca-rich core in some garnet (Fig. 11b) is mantled by Ca-poor areas. Rims are Ca-rich and show partial resorption. Mn first increases in Ca-rich rims and decreases again in the external, Ca-richest parts of the rims. More classical concentric zoning with Mn-rich core and Ca-rich rims is also observed (Fig. 11c), also with limited resorption. Garnet from the lower-grade section (found in veinlets in metacherts along the Cascapedia river, samples MA-14-24 and MA-14-31 on Fig. 11a) has higher pyrope (sample MA-14-31) and grossular (sample MA-14-24) content.

Biotite has X_{Mg} in the range 0.45-0.65, with highest Ti content associated with X_{Mg} ~0.55 (Fig. 11d).

Feldspars consist of orthoclase and plagioclase varying between oligoclase and andesine (Fig. 11e).

Phengite is generally muscovite-rich (Fig. 11f) with up to 18% Tschermak substitution towards celadonite and limited pyrophyllitic substitution (≤ 6% for most analyses).

Staurolite composition shows negligible solid solution with Mn (≤ 0.2 MnO wt. %) and has X_{Mg} in the range 0.15-0.25, for crystals included in garnet as well as in the foliation. Staurolite at an angle with the foliation (Fig. 6g) and growing over garnet is homogeneous around X_{Mg} = 0.20.

Scapolite is a sodian meionite with Si = 7.17 apfu and Ca / (Ca+Na) = 0.71 when structural formula is calculated to compensate 50 negative charges (C and Cl were not measured).

As for mafic rocks, chlorite is a chamosite with low sudoite content. It has X_{Mg} between 0.39 and 0.52, lower than for mafic rocks but similar Si content in the range 2.55-2.65 apfu.

6. PHASE EQUILIBRIA AND THERMOBAROMETRY

The petrological evolution of the sole is modelled here with the use of a pseudosection (phase diagram for fixed bulk rock composition) representative of the mafic rocks. Despite progress in the thermodynamic models for mafic compositions, uncertainties remain large for thermobarometry on these rocks, especially compared to mineral assemblages in metapelites. To further constrain conditions of crystallisation, we carried out empirical thermobarometry on all lithologies and multi-equilibrium thermobarometry on selected assemblages in metapelites. This approach has been preferred over building pseudo-sections as the observed metapelites are very thin beds (up to ~10 cm thick within the mafic rocks) showing poly-metamorphic history with compositional banding, retrogression and evidence for opening of the system and interaction with the mafic rocks. Therefore assuming equilibrium at sample scale and close system has been deemed erroneous for the metapelites.

6.1. Mafic rocks

6.1.1.Phase equilibria

Figure 11 shows a pseudo-section modelled in the NCKFMASHTO system for the high-grade subunit, using THERMOCALC version 3.45 (Holland and Powell, 1998, 2011) with the updated database version (tc-ds62) of Holland and Powell (2011). The selected bulk rock composition is an average of six samples of the garnet amphibolite measured by O'Beirne-Ryan et al. (1990), which has been deemed representative of the large-scale composition of the high-grade subunit, reducing sampling biases due to compositional banding. Water content was calculated through mass balance of amphibole proportion over several thin sections and corresponds within error to the average loss on ignition obtained by O'Beirne-Ryan et al. (1990). Activity models are after White et al. (2014b) for orthopyroxene, biotite, chlorite and garnet, Green et al. (2016) for mafic melts, augite and hornblende, Holland and Powell (2003) for plagioclase and K-feldspar, and White et al. (2000) for ilmenite-

464hematite. In the absence of magnetite or any other Fe^{3+} rich phase at peak conditions, rock oxidation
465was set to 1 %, following previous studies on similar rocks (e.g., Guilmette et al., 2011; Palin et al.,
4662014).

467Peak conditions were approximated based on the observed mineralogy and isopleths for garnet
468(grossular fraction and X_{Fe} = Fe/(Mg+Fe), all in apfu), clinopyroxene (X_{Fe}), and amphibole (X_{Fe}), using
469representative mineral compositions for the large, homogeneous crystal cores (not the symplectites)
470given by O'Beirne-Ryan et al. (1990) and measured in this study. Garnet, clinopyroxene and
471amphibole are stable throughout the pseudosection, with the amphibole-out reaction at temperatures
472greater than 1000°C, which is consistent with the dehydration reaction of hornblende (Wolf and
473Wyllie, 1994). Pressure-temperature conditions for the field best matching the mineralogy for the
474high-grade subunit are around 0.98 ± 0.04 GPa and 825 ± 25°C (Fig. 12). They lie at supra-solidus
475conditions where rutile is stable. Plagioclase is not predicted at peak conditions, also consistently with
476observations where plagioclase is only very rarely found other than associated to the symplectites. In
477this pseudosection, the plagioclase field does not extend to pressures above 0.8 GPa. Estimated modes
478are in good agreement with sample modes for amphibole (44%), clinopyroxene (20%) and garnet (26
479%), as for sample MA-14-35 (Fig. 4b). A melt proportion of 9 vol.% is predicted and broadly
480consistent with previous estimates for mafic rocks at comparable conditions using similar activity
481models (Palin et al., 2016 ; Soret et al., 2017). The Ti content of amphibole (0.08 apfu) is close to that
482reported by O'Beirne-Ryan et al. (1990) (0.10 apfu), but in the low range of values document in this
483study (0.05 up to 0.20 apfu; Fig. 9b). The X_{Fe} of amphibole at ~0.32 compares well with the
484compositions observed here and given by O'Beirne-Ryan et al. (1990).

485 *6.1.2. Garnet-clinopyroxene thermometry*

486Garnet-clinopyroxene thermometry has been carried out on the two samples (MA-14-35 and MA-14-
48738) where phase relations between garnet and clinopyroxene are clearest. In both cases garnet and
488clinopyroxene are zoned, with relatively large, homogenous cores and variably-sized rims linked to
489the garnet-clinopyroxene-epidote-plagioclase symplectite. Equilibrium is inferred between garnet and
490clinopyroxene cores, and between minerals in the symplectitic rim. The Fe-Mg distribution coefficient

$\left(K_D = \frac{Fe^{2+}_{Grt} . Mg^{\square}_{Cpx}}{Fe^{2+}_{Cpx} . Mg^{\square}_{Grt}}\right)$ increases from core pairs (in the range K_D = 3.5 - 5) to rim pairs ($K_D \geq 7$). Figure 2 shows the results of four empirical thermometers. The first three (Ellis and Green, 1979; Powell, 1985; Krogh Ravna, 1988) give consistently higher temperatures than the more recent thermometer of Krogh Ravna (2000) which is retained, as it specifically addresses possible over-estimation by the other three thermometers in this type of samples. Selected crystallisation temperatures vary between 820 and 900°C for equilibrium between garnet-clinopyroxene cores and between 680 and 720°C for equilibrium between rims.

6.1.3.Amphibole-plagioclase thermometry

The amphibole–plagioclase thermometer of Holland and Blundy (1994) has been used on two samples (MA-14-38, MA-14-42) from the high-grade amphibolite and four samples (MA-14-22, 23, 26, 32) from the amphibolite of the low-grade unit. For the high-grade unit, equilibrium is inferred between pargasitic amphibole and anorthitic plagioclase (Fig. 9). For the low-grade unit, equilibrium is inferred between amphibole rim composed of Mg-hornblende and plagioclase of andesine type with anorthite content of 23% (Fig. 9). Pressure was assumed constant at 0.95 GPa. This method gave two clusters separated by ~200°C: the high-grade amphibolite yielded estimates of 875±40°C and the low-grade amphibolite yielded estimates of 680±40°C.

6.2. Metapelites

Multi-equilibrium thermobarometry has been carried out on selected mineral assemblages in metapelites. Three main parageneses have been recognized and tested for thermodynamic equilibrium:

- kyanite – garnet cores – quartz – biotite – staurolite as seen in garnet inclusions (e.g. Fig. 6), for the prograde history
- aluminosilicate – garnet mantle – plagioclase – biotite – quartz with kyanite or sillimanite depending on sample, for peak metamorphic conditions
- sillimanite – staurolite – phengite, all crosscutting the foliation and associated in sample MA-15-5a (Fig. 6f-h).

Multi-equilibrium thermobarometry was carried out using THERMOCALC (Holland and Powell, 1998, 2011) version 3.33 with the thermodynamic database tc-ds55. Results are summarised in figure

514. For sample MA-15-5a, the peak mineral assemblage garnet + biotite + muscovite + plagioclase + quartz + sillimanite gives estimates of 690 ± 27°C and 0.85 ± 0.1 GPa. For sample MA-14-50, the assemblage garnet + biotite + muscovite + plagioclase + quartz + kyanite yields conditions of 750 ± 30°C and 0.92 ± 0.1 GPa. The same assemblage in sample MA-14-48a gives peak conditions of 615 ± 65°C and 1.2 ± 0.4 GPa. For this sample, addition of staurolite (included in garnet with kyanite and biotite) refines estimates for prograde metamorphism at 633 ± 32°C and 1.1 ± 0.17 GPa. For the staurolite and aluminosilicate-free sample MA-14-52, the assemblage garnet + biotite + muscovite + plagioclase + quartz yields 640 ± 40°C and 1.01 ± 0.14 GPa.

Chlorite-phengite thermobarometry could not be systematically carried out due to the generally low sudoite content of the chlorite, which nevertheless indicates that chlorite likely crystallised over 350°C (see Bourdelle and Cathelineau, 2015). Chlorite thermometry (using the approach and thermodynamic properties given in Vidal et al., 2006) yields values of 457°C and 496°C for two groups of chlorite in sample MA-14-22, a mafic rock in the low-grade section of the sole. Unfortunately no phengite at equilibrium were identified in this sample, therefore corresponding pressure could not be estimated.

The Ti-in-biotite thermometer of Henry et al. (2005) yields estimates of 695 ± 23°C and 680 ± 23°C for the samples MA-15-5a and MA-14-50, respectively. The garnet-biotite thermometer of Holdaway (2000) gives estimates of 700 ± 25°C for these samples. Additional pressure estimates in metapelites were obtained using the garnet-biotite-muscovite-plagioclase barometers of Wu (2015), yielding 0.8 ± 0.12 GPa and 0.91 ± 0.12 GPa for samples MA-15-5a and MA-14-50. These are within uncertainties of the garnet-biotite-muscovite-aluminosilicate-quartz barometer of Wu and Zhao (2007), yielding 0.7 ± 0.08 GPa and 0.88 ± 0.08 GPa for samples MA-15-5a and MA-14-50, not shown on figure 14 for readability.

In the low-grade unit, the Ti-in-biotite thermometer gives 610 ± 23°C for the sample MA-14-24 (the only biotite-bearing sample in this subunit). In sample MA-14-31, the Ti-in- muscovite thermometer of Wu and Chen (2015) yields 515 ± 65°C, within uncertainties of the garnet-muscovite thermometer of Wu and Zhao (2006) at 555 ± 16°C on the same sample.

7. DISCUSSION

7.1. Petrological evolution of the metamorphic sole

7.1.1.Nature of the protolith

Close to the contact with the peridotite, metamorphic sole rocks are strained, sheared and lack relicts of original magmatic minerals so that the original nature of the rock is hard to assess: although the high-grade unit is indisputably of mafic origin, whether these rocks were gabbros or basalt-type lavas could not be deciphered. The presence of metasediments in the high-grade unit advocates oceanic floor origin, and the persistence of (strained) boudins and spherulites in the folded, lower-grade unit suggests basaltic lavas with a shallow oceanic crust origin, together with the absence of relicts of gabbro-derived clinopyroxene. This is consistent with a single geodynamic origin for the metamorphic sole, with the metasedimentary content increasing away from the structural top (as discussed by Agard et al., 2016). In this view the metamorphic sole of the Mont Albert ophiolitic complex represents a subducted portion of the Schick-Schock group units, which is consistent with the similarities in compositions reported for both mafic lithologies (O'Beirne-Ryan et al., 1990; Camiré et al., 1995).

7.1.2.Pressure-temperature history of the samples

Thermobarometric estimates carried out in this study are compiled in figure 14. For the high-grade unit, pressure estimates on metapelites cluster within uncertainties and indicate crystallisation pressures around 0.95(+/-0.10) GPa. Calculated temperatures range between 650°C and 950°C, with garnet-clinopyroxene estimates using crystal cores being highest in sample MA-14-38 and seemingly somewhat overestimated. Broadly speaking, mafic samples close to the contact with peridotites have reached temperatures between 850 and 900°C.

Estimates at lower temperatures for these samples, such as garnet-clinopyroxene rims, are interpreted as indicative of cooling along the retrograde path. Metasediments were not found less than ~25 m away from the contact and indicate lower temperatures in the range 750-650°C, matching crystallisation of the garnet-clinopyroxene rims. Kyanite and staurolite inclusions in garnet show that prograde metamorphism took place in the field of kyanite and staurolite, along a geothermal gradient of the order of 20°C/km (sample MA-14-52). For the lower-grade unit rocks, further away from the contact, estimated temperatures are distinctly lower than close to the contact, with some overlap with the lowest peak temperatures estimated in the high-range unit (~700°C).

In rocks from the lower-grade unit, equilibrium was probably not reached at sample scale at peak temperature, given that amphibole preserves Al-poor cores interpreted as crystallising along the prograde path. In these samples chlorite geothermometry gives temperatures below 500°C which are interpreted as crystallisation temperatures during cooling. Crystallisation pressures here are poorly constrained, apart from the lack of evidence of high-pressure or very-low pressure index minerals. Tectonic juxtaposition of the low- and high-grade units and peak metamorphic conditions of the low-grade unit suggest a retrograde path along a similar geothermal gradient for both units.

These results are consistent with step-wise accretion of two (or more) subunits of metamorphic soles. These units (and/or samples within the subunits) *do not* share an identical pressure-temperature path, as suggested by Gagnon and Jamieson (1986). Metamorphic rocks close to the contact with the peridotites record higher temperatures than further away, either because of step-wise accretion of subunits or due to slow thermal equilibration compared with exhumation. The obtained pressure-temperature paths appear clockwise, with burial largely in the field of kyanite and exhumation starting in that of sillimanite.

7.1.3. Compositional evolution and stability of epidote

The broad compositional range of epidote and its links with texture (with Al-rich cores and Fe^{3+}-rich rims and late veins, Fig. 7 and 10), mineral assemblage and distance to the contact, allow further constraining the petrological history of the metamorphic sole. The composition of epidote is known to vary with temperature and oxygen fugacity (fO_2), where increasing fO_2 leads to increase the stability field of epidote towards higher temperature (e.g. Holdaway, 1972). In metasomatic veinlets from the garnet-bearing amphibolite with epidote-corundum assemblage (sample MA-14-2b, Fig. 6d-e and 10), the pistacite component of epidote is about 0.5. This indicates a maximum crystallisation temperature around 700°C (Holdaway, 1972). Variations of composition in the high-grade subunit where the Fe^{3+} content of epidote increases at the expense of Al from crystal cores to rims (Fig. 7d) then to late veins (Fig. 10) are consistent with decreasing crystallisation temperatures as indicated by the clinozoisite component (Schmidt and Poli, 2004).

The texture of clinozoisite-rich epidote and its association to garnet, clinopyroxene, plagioclase and oxide in the symplectite point to high-grade metamorphic conditions. The presence of clinozoisite-rich

epidote may reflect the involvement of magmatic fluids, as MORB melting gives epidote up to 800-830°C at 0.9-1.2 GPa (see review of Schmidt and Poli, 2004) and magmatic epidote is also mentioned in comparable assemblages with similar texture by Lardeaux and Spalla (1991) and Nicollet et al. (1979). Higher temperature for epidote crystallisation in metamorphic soles is not impossible as fO_2 and water content are only inferred here, and zoisite may have been missed in the field. The amphibole-epidote-plagioclase-garnet assemblage is nevertheless regarded as representative of conditions around 0.9-1.5 GPa and 700-830°C for reasons given by Schmidt and Poli (2004), in good agreement with present thermobarometric estimates.

7.2. Formation and structure of the metamorphic sole

7.2.1.Metamorphic sole and subduction initiation

The metamorphic sole of the Mont Albert ophiolitic complex appears broadly similar to other metamorphic soles, hinting at a common formation process. The overall structure and petrology reproduce that of the Semail ophiolite, yet with smaller differences between metamorphic grades for the base of the high-grade unit and the top of the low-grade unit. However differences in deformation between high and low-grade units are as striking as in the Semail ophiolite, where the low-grade unit is thickened by numerous folds and faults (Hacker and Mosenfelder, 1996; Gray and Gregory, 2000). Here, aluminous metasediments allow more accurate estimation of peak metamorphic pressure, and confirm broadly similar peak conditions. Peak temperatures are in the range of those estimated in Semail (~850°C), and compare well with estimations for the sole of the Bay of Islands complex, where sillimanite is also reported (e.g., Suhr and Cawood, 1993). These estimates all fall well into stability conditions of a metabasalt-derived melt (Fig. 12). In the model of Agard et al. (2016), subducted metabasalts (future metamorphic soles) are “underplated” (accreted to upper plate peridotites) when both units have similar effective viscosities and coupling is maximal between the two. Agard et al. (2016) emphasize that conditions allowing accretion of the metamorphic sole are only transiently met, because of the general cooling of the subduction system. This restricts the origin of the high-grade section of the metamorphic sole to the tip of the forming slab (see Fig. 1a-b), and implies that the mixed mafic-sedimentary protolith deposited close to the future trench – and further away from the

continental margin than presented in e.g. the geodynamic reconstruction of Tremblay and Pinet (2016, their figure 19).

Figure 15 compares peak metamorphic conditions estimated in this study to the thermal structure of oceanic lithosphere over time, from present-time modelling. Peak metamorphic conditions of 800 to 900°C in the metabasalt at ~33 km depth imply that the overriding oceanic lithosphere was less than about 20 My-old. This is a maximum age as cooling of the slab/mantle interface due to slab penetration would imply a younger age. The reconstructed ~33 km depth has geodynamic implications for the distance of the trench/megathrust to the ridge. Assuming subduction took place at a convergence rate of 2 cm/yr (consistent with kinematics estimated by e.g. Bradley, 1989) with a 25° dip of the slab indicates that ~4 Ma were necessary to subduct the high-grade metabasalts to peak pressure, which decreases to ~2.3 Ma for a 45° slab dip. In any case the time required to bury mafic rocks of the future metamorphic sole to peak pressure is not insignificant but small compared to the age of the overriding lithosphere during underplating of the sole. This time lapse is short yet sufficient for heat transfer to the whole high-grade unit (always thinner than 100 m, to be compared with the much larger lengths heat may travel in a Ma, e.g. Bickle and McKenzie, 1987). Overall, this model is consistent with subduction initiating close to (within tens of kilometres) or at the ridge and with metamorphic soles originating from ocean-floor rocks located close to the forming trench at the time of subduction initiation (also within tens of kilometres). Greater distances, convergence rates below cm/yr and shallow slab dipping require greater time for burial to peak pressure and become inconsistent with the thermal structure of oceanic lithosphere shown in figure 15a due to cooling of the mantle wedge. The supra-subduction zone origin of the ophiolitic complex proposed by many authors (see Tremblay et al., 2011) suggests that the oceanic lithosphere where subduction initiated (within the Iapetus ocean) could have been warmer than presented in figure 15a. This resonates with the global scale analysis of Vaughan and Scarrow (2003) who link thermal rejuvenation of the oceanic lithosphere to ophiolite obduction. Unfortunately testing for thermal rejuvenation is beyond the resolution of the geological record of the Mont Albert ophiolitic complex, especially as peridotites remain too poorly dated to compare with peak metamorphism ages in the sole.

7.2.2.Clockwise pressure-temperature paths in a cooling geodynamic environment

The mineral record of the Mont Albert metamorphic sole argues for hair-pin yet clockwise pressure-temperature paths with exhumation along a warmer geothermal gradient than during burial. Although this is counter-intuitive, given the progressive cooling of the plate interface (and the trajectories of Hacker and Gnos, 1997), this is explained by rapid vertical movements in comparison of thermal re-equilibration of the overriding plate, as tentatively depicted in figure 15b-c.

Figure 15b and c show ocean-floor basalts buried below the plate interface, in a nascent subduction zone concomitantly of downward advection of isotherms (heating below the plate interface is comparatively slow: step 1 on Fig. 15b-c). Over time, isotherms in the lower plate are increasingly parallel to the plate interface. The thermal gradient through the plate interface to the upper plate increases with time, explaining the near-isobaric temperature increase of the high-grade unit during its accretion (step 2 on Fig. 15b-c). Exhumation follows along the base of the upper plate together with peridotites. Through the still sharp temperature gradient, exhumation explains initially rapid cooling (step 3) continuing along a warmer thermal gradient than burial (via step 4). With time, the plate interface has been cooling significantly (compare isotherms at t1 and t4). This schematic model is only valid if the upper plate remains significantly warmer over a distance of several tens of meters above the plate interface during the time of exhumation of the metamorphic sole (i.e. a few millions years, in agreement with radiometric constraints discussed above). Preservation of peak temperature mineral assemblages above 700°C and of subsequent parageneses without homogenization by diffusion are also consistent with fast cooling.

7.2.3.Melting… or not?

In the Mont Albert ophiolitic complex, absence of metasediments from the rocks less than 20 metres away from to the contact with the peridotite is observed in a trend where the proportion of sediments and their quartz content apparently increase towards the base of the sole. This has also been noted in the Semail metamorphic sole (e.g. Soret et al., 2017). In their model, Agard et al. (2016) point out that ocean-floor derived subducted rocks likely contain more sediments with time as distance to the margin decreases (following closure of the basin).

Alternatively, the absence of metasediments from the first 20 metres may be related to melting: close to the contact, metamorphic conditions are well above 700°C and aluminous metapelites should have

been molten at a significant degree (>30 %), consistently with observations of geochemical tracers of subducted sediments within arc magmas (e.g. Labanieh et al., 2012; Plank et al., 2009). Melts produced from the metasediments and from the amphibolite should have near granitic composition at peak conditions (see Feisel et al., 2018 for open system amphibolite melting at 0.95 GPa) and should produce easily identifiable leucosomes. However leucosomes and melt remnants are rare throughout the sole and have not been found closer than about 20 metres from the contact or crosscutting the peridotite. The restite of molten sediments may have been missed in the field (it is probably dark within dark mafic rocks), especially as shearing has been intense and proportions of metasediments are small in comparison to mafic rocks. Corundum-epidote-chlorite rocks found within the amphibolite less than 10 metres away from the contact may record interactions between partially molten metapelites and mafic rocks, but these are rare and cryptic.

Generalized partial melting is predicted in all present rock types above 750°C. Soret et al. (2017) argue that limited melting of the metabasalts may enhance accretion, with a threshold around 7% partial melting, above which melting would cause too much weakening to allow accretion. This suggests that metasediment-derived melts were mostly extracted parallel to the slab, and/or that melt-rich lithologies were not accreted to the upper plate peridotite and subsequently subducted and lost to the mantle. In this view, the absence of metasediments close to the contact would be explained (in the model of Agard et al., 2016) as due to a too large decrease in effective viscosity (because of melting) to allow coupling and accretion to the upper plate. It follows that what has been identified as the high-grade metamorphic sole unit could be a more complex assemblage of small (tens of metres in thickness at most) subunits, as in the Semail metamorphic sole (Soret et al., 2017). A possible consequence is that mafic rocks located immediately at the contact with the peridotite and lacking metapelites could have formed at higher pressure than estimated here (since pressure is possibly estimated with larger uncertainties in mafic rocks). Pressure estimates in horizons with pelitic and mafic lithologies nevertheless concur (e.g., figure 14a).

8. CONCLUSION

The metamorphic sole of the Mont Albert ophiolitic complex and its relicts of metasediments provide clues to understand early subduction dynamics. As for the Semail ophiolite, a strong, seemingly

712inverted metamorphic gradient is observed within the two main subunits respectively characterized by
713granulite / higher amphibolite facies and higher greenschist facies metamorphism. The metamorphic
714sole appears derived from the Schick-Shock volcanics from the Dunnage zone, and its petrology
715suggests a shallow, ocean-floor origin (basalt and sediments, although the absence of gabbro is hard to
716prove unequivocally).
717Limited retrogression and presence of aluminous metapelites allow constraining the metamorphic
718history of the high-grade unit to peak pressure around 0.95 GPa with peak temperatures up to about
719850°C. These estimates are consistent with the model proposed by Agard et al. (2016), where the
720metamorphic sole formed in a nascent subduction zone, below young (less than ~20 Ma) or
721rejuvenated oceanic lithosphere, with burial along a geothermal gradient around 20°C/km. This study
722provides evidence for a clockwise metamorphic path, with exhumation of the high-grade units along a
723warmer geothermal gradient (~40°C/km), suggesting rapid exhumation (i.e., faster than thermal re-
724equilibration and cooling of the mantle wedge above the plate interface). Cooling of the interface is
725documented by successive underplating of subunits with progressively lower peak metamorphic
726conditions (away from the contact with the peridotite). The necessarily fast pace of evolution of the
727metamorphic sole of the Mont Albert ophiolitic complex (formation below warm oceanic lithosphere,
728underplating and exhumation) is consistent with the narrow range of ages obtained by Tremblay et al.
729(2011) for the Thetford-Mines ophiolitic complex along the same suture zone: oceanic magmatism (at
730~480 Ma), formation of the high-grade metamorphic sole (at ~476 Ma), emplacement of sole-derived
731melting products in the peridotite (at ~470 Ma) and cooling of the metamorphic sole (from ~466 Ma to
732the end of obduction around 460 Ma), all took place within ~20 Ma. Although partial melting is
733reported in Taconian ophiolitic soles (e.g. at the Thetford-Mines ophiolite: Tremblay et al., 2011; the
734Bay of Islands complex: Suhr and Cawood, 1993), evidenced in metapelites and predicted by
735thermodynamic modelling in mafic rocks (up to ~9 vol.%) at the Mont Albert ophiolitic complex, melt
736remnants such as leucosomes, granitoids or felsic intrusions are sparse. This may relate to strain
737localization in melt-rich lithologies, precluding coupling and favouring accretion of the mafic
738lithologies now found close to the contact with the overlying peridotite. Strain localisation during
739melting and melt drainage appear linked to stepwise accretion of subunits to form metamorphic soles,

consistently with pulsatile melting during prograde metamorphism (e.g. Diener and Fagereng, 2014) and with similar mechanisms observed in the metamorphic sole of the Semail ophiolite (Soret et al., 2017).

ACKNOWLEDGEMENTS

This work was financially supported by the CNRS INSU programs, by the ON:LAP project (ANR blanche, SIMI6; 2010 BLAN 615 01) and by ISTeP. We thank L. Labrousse for his help in organizing field trips; O. Boudouma for his expertise with SEM characterisation; M. Fialin and N. Rividi for help with EPMA; A. Le Meur, C. Finco and A. Rambert for their careful work on mineralogy during internships; B. Lefeuvre for his help during the second field trip; A. Plunder and C. Prigent for fruitful discussions. We are also indebted to C. Isabel and M. L'Italien from SEPAQ for authorizing access to restricted areas and for their kind help and advice during field trips for reaching outcrops. Constructive comments on the first version of the manuscript by J. Wakabayashi, P. Lanari, an anonymous reviewer and editor T. Pettke are gratefully acknowledged.

REFERENCES

Alcock F J. (1927). La région cartographiée du Mont Albert, Québec; Memoir no. 144 of the Geological Survey of Canada, 79 pages (plus 2 sheets) doi:10.4095/119929

Agard P., Searle M. P., Alsop G. I., Dubacq B. (2010). Crustal stacking and expulsion tectonics during continental subduction: P-T deformation constraints from Oman. *Tectonics* **29**, TC5018. doi: 10.1029/2010TC002669

Agard P., Yamato P., Soret M., Prigent C., Guillot S., Plunder A., Dubacq B., Monié P. & Chauvet A. (2016). Plate interface rheological switches during subduction infancy: control on slab penetration and metamorphic sole formation. *Earth Planetary Science Letters* **451**, 208-220.

Beaudin J. (1983). Analyse structurale du groupe ShickShock et de la péridotite alpine du Mont Albert, Gaspésie. Ph.D. thesis, Université Laval, Sainte-Foy (Québec).

Boudier F., Nicolas, A. & Bouchez, J. L. (1982). Kinematics of oceanic thrusting and subduction from basal sections of ophiolites. *Nature* **296**, 825-828.

Bourdelle F. & Cathelineau M. (2015). Low-temperature chlorite geothermometry: a graphical representation based on a T–R^{2+}–Si diagram. *European Journal of Mineralogy* **27**, 617-626.

768 Bradley D. C. (1989). Taconic Plate kinematics as revealed by foredeep stratigraphy,
769Appalachian Orogen. *Tectonics* **8**, 1037-1049.

770 Bucher K., de Capitani C. & Grapes R. (2005). The development of a margarite–corundum
771blackwall by metasomatic alteration of a slice of mica schist in ultramafic rock, Kvesjøen, Norwegian
772Caledonides. *The Canadian Mineralogist* **43**, 129-156.

773 Camiré G., La Flèche M. & Jenner G. (1995). Geochemistry of pre-Taconian mafic volcanism in
774the Humber Zone of the northern Appalachians, Québec, Canada. *Chemical Geology* **119**, 55-77.

775 Cawood P. A. & Suhr G. (1992). Generation and obduction of ophiolites: Constraints from the
776Bay of Islands Complex, western Newfoundland. *Tectonics* **11**, 884-897.

777 Cesare B., Acosta-Vigil A., Bartoli O. & Ferrero S. (2016). What can we learn from melt
778inclusions in migmatites and granulites? *Lithos* **239**, 186-216.

779 Cowan R. J., Searle M. P. & Waters D. J. (2014). Structure of the metamorphic sole to the Oman
780Ophiolite, Sumeini Window and Wadi Tayyin: implications for ophiolite obduction processes.
781*Geological Society of London, Special Publication* **392**, 155-175.

782 Dewey J. F. (1976). Ophiolite obduction. *Tectonophysics* **31**, 93-120.

783 De Souza S., Tremblay A., Ruffet G. & Pinet N. (2012). Ophiolite obduction in the Quebec
784Appalachians, Canada - 40Ar/39Ar age constraints and evidence for syn-tectonic erosion and
785sedimentation. *Canadian Journal of Earth Sciences* **49**, 91-110.

786 De Souza S., Tremblay A. & Ruffet G. (2014). Taconian orogenesis, sedimentation and
787magmatism in the southern Quebec–northern Vermont Appalachians: Stratigraphic and detrital
788mineral record of Iapetan suturing. *American Journal of Science* **314**, 1065-1103.

789 Diener J. F. A. & Fagereng Å. (2014). The influence of melting and melt drainage on crustal
790rheology during orogenesis. *Journal of Geophysical Research: Solid Earth* **119**, 6193-6210.

791 Dimo-Lahitte A., Monié P. & Vergély P. (2001). Metamorphic soles from the Albanian
792ophiolites: Petrology, 40Ar/39Ar geochronology, and geodynamic evolution. *Tectonics* **20**, 1, 78–96.

793 Duretz T., Agard P., Yamato P., Ducassou C., Burov E. & Gerya T. V. (2016). Thermo-
794mechanical modeling of the obduction process based on the Oman Ophiolite case. *Gondwana*
795*Research* **32**, 1-10.

796 Ellis D. & Green D. (1979). Experimental-study of the effect of Ca upon garnet-clinopyroxene
797Fe-Mg exchange equilibria. *Contributions to Mineralogy and Petrology* **71**, 13-22.

798 Feisel Y., White R. W., Palin R. M. & Johnson T. E. (2018). New constraints on granulite facies
799metamorphism and melt production in the Lewisian Complex, northwest Scotland. *Journal of*
800*Metamorphic Geology* **36**, 6, 799-819.

801 Gagnon Y.D. & Jamieson R.A. (1986). Étude de la semelle métamorphique du complexe du
802Mont Albert, Gaspésie, Québec. *Commission géologique du Canada, Current Research part*
803*B/Recherches En Cours Partie B;* Études no. 86-1B, 1-10, doi: 10.4095/120623

804 Gnos E. (1998). Conditions of Garnet Amphibolites Beneath the Semail Ophiolite: Implications
805for an Inverted Pressure Gradient. *International Geological Review* **40**, 281-304.

806 Gray D. R. & Gregory R. T. (2000). Implications of the structure of the Wadi Tayin metamorphic
807sole, the Ibra-Dasir block of the Samail ophiolite, and the Saih Hatat window for late stage extensional
808ophiolite emplacement, Oman. *Marine Geophysical Research* **21**, 211-227.

809 Green E. C. R., White R. W., Diener J. F. A., Powell R., Holland T. J. B. & Palin R. M. (2016).
810Activity-composition relations for the calculation of partial melting equilibria in metabasic rocks.
811*Journal of Metamorphic Geology* **34**, 845-869.

812 Guilmette C., Indares A. & Hébert R. (2011). High-pressure anatectic paragneisses from the
813Namche Barwa, Eastern Himalayan syntaxis: Textural evidence for partial melting, phase equilibria
814modeling and tectonic implications. *Lithos* **124**, 66–81.

815 Gueddari K., Flèche M. R. L. & Camiré G. (1999). Premières données sur la géochimie des
816éléments du groupe du platine (EGP) dans les péridotites du mont Albert (Québec). *Comptes Rendus*
817*de l'Académie des Sciences - Series IIA* **329** 479-486,

818 Hacker B. R. (1991). The role of deformation in the formation of metamorphic gradients: Ridge
819subduction beneath the Oman Ophiolite. *Tectonics* **10**, 455-473.

820 Hacker B. R. & Gnos E. (1997). The conundrum of Samail: explaining the metamorphic history.
821*Tectonophysics* **279**, 1, 215-226.

822 Hacker B. R. & Mosenfelder J. L. (1996). Metamorphism and deformation along the
823emplacement thrust of the Samail ophiolite, Oman. *Earth Planetary Science Letters* **144**, 435-451.

824 Hacker B. R., Mosenfelder J. L. & Gnos E. (1996). Rapid emplacement of the Oman ophiolite:
825Thermal and geochronologic constraints. *Tectonics* **15**, 1230-1247.

826 Holdaway M. J. (1972). Thermal stability of Al-Fe epidote as a function of fO_2 and Fe content.
827*Contributions to Mineralogy and Petrology* **37**, 307-340.

828 Holdaway M. J. (2000). Application of new experimental and garnet Margules data to the garnet-
829biotite geothermometer. *American Mineralogist* **85**, 881.

830 Henry D. J., Guidotti C. V. & Thomson J. A. (2005). The Ti-saturation surface for low-to-
831medium pressure metapelitic biotites: Implications for geothermometry and Ti-substitution
832mechanisms. *American Mineralogist* **90**, 2-3, 316-328.

833 Holland T. J. B. & Blundy J. (1994). Non-ideal interactions in calcic amphiboles and their
834bearing on amphibole-plagioclase thermometry. *Contributions to Mineralogy and Petrology* **116**, 433-
835447.

836 Holland T. J. B. & Powell R. (1998). An internally-consistent thermodynamic dataset for phases
837of petrological interest. *Journal of Metamorphic Geology* **16**, 309-344.

838 Holland T. J. B. & Powell R. (2003). Activity-composition relations for phases in petrological
839calculations: an asymmetric multicomponent formulation. *Contributions to Mineralogy and Petrology*
840**145**, 4, 492-501.

841 Holland T. J. B. & Powell R. (2011). An improved and extended internally consistent
842thermodynamic dataset for phases of petrological interest, involving a new equation of state for solids.
843*Journal of Metamorphic Geology* **29**, 333-383.

844 Ishikawa T., Fujisawa S., Nagaishi K. & Masuda T. (2005). Trace element characteristics of the
845fluid liberated from amphibolite-facies slab: Inference from the metamorphic sole beneath the Oman
846ophiolite and implication for boninite genesis. *Earth Planetary Science Letters* **240**, 355-377.

847 Jamieson R. A. (1986). P-T paths from high temperature shear zones beneath ophiolites. *Journal*
848*of Metamorphic Geology* **4**, 3-22.

849 Kohn M. J. (2003). Geochemical zoning in metamorphic minerals. In: Holland, H. D. &
850Turekian, K. K. (eds.) Treatise on Geochemistry. Oxford: Pergamon, pp. 229–261.

851 Krogh Ravna E. J. (1988). The garnet-clinopyroxene Fe-Mg geothermometer - a reinterpretation
852of existing experimental-data. *Contributions to Mineralogy and Petrology* **99**, 44-48.

853 Krogh Ravna E. J. (2000). The garnet–clinopyroxene Fe^{2+}–Mg geothermometer: an updated
854calibration. *Journal of Metamorphic Geology* **18**, 211-219.

855 Labanieh S., Chauvel C., Germa A. & Quidelleur X. (2012). Martinique: a Clear Case for
856Sediment Melting and Slab Dehydration as a Function of Distance to the Trench. *Journal of Petrology*
857**53**, 12, 2441-2464.

858 Laurent R. & Hebert Y. (1979). Paragenesis of serpentine assemblages in harzburgite tectonite
859and dunite cumulate from the Quebec Appalachians. *The Canadian Mineralogist* **17**, 857-869.

860 Lardeaux J. M. & Spalla M. I. (1991). From granulites to eclogites in the Sesia zone (Italian
861Western Alps): a record of the opening and closure of the Piedmont ocean. *Journal of Metamorphic*
862*Geology* **9**, 35-59.

863 Leake B. E., Woolley A. R., Arps C. E. S., Gilbert M. C., Grice J. D., Hawthorne F. C., Kisch H.
864J., Krivovichev V. G., Canada J. A. M., Maresch W. V., Schumacher J. C., France D. C. S.,
865Stephenson N. C. N. & Whittaker E. J. W. (1997). Nomenclature of amphiboles. *Canadian*
866*Mineralogist* **35**, 219-246.

867 Linckens J., Herwegh M. & Müntener O. (2011). Linking temperature estimates and
868microstructures in deformed polymineralic mantle rocks. *Geochemistry, Geophysics, Geosystems* **12**,
8698, doi: 10.1029/2011GC003536.

870 Lux D. R. (1986). $^{40}Ar/^{39}Ar$ ages for minerals from the amphibolite dynamothermal aureole, Mont
871Albert, Gaspé, Quebec. *Canadian Journal of Earth Sciences* **23**, 1, 21–26.

872 MacGregor I. D. (1964). A study of the contact metamorphic aureole surrounding the Mount
873Albert ultramafic intrusion [Ph.D. dissert.] Princeton, New Jersey, Princeton University, 195 p.

874 MacGregor I. D. & Basu A. R. (1979). Petrogenesis of the Mount Albert Ultramafic Massif,
875Quebec *Geological Society of America Bulletin* **90**, 1529-1627.

876 Mahmood K., Boudier F., Gnos E., Monié P. & Nicolas A. (1995). $^{40}Ar/^{39}Ar$ dating of the
877emplacement of the Muslim Bagh ophiolite, Pakistan. *Tectonophysics* **250**, 169 – 181.

878 Malo M., Cousineau P. A., Sacks P. E., Riva J. F., Asselin E. & Gosselin P. (2001). Age and
879composition of the Ruisseau Isabelle Mélange along the Shickshock Sud fault zone: constraints on the
880timing of mélanges formation in the Gaspé Appalachians. *Canadian Journal of Earth Sciences* **38**, 21-
88142.

882 Malo M., Ruffet G., Pincivy A. & Tremblay A. (2008). A 40Ar/39Ar study of oceanic and
883continental deformation processes during an oblique collision: Taconian orogeny in the Quebec
884reentrant of the Canadian Appalachians. *Tectonics* **27**, TC4001.

885 Martin J.-P. & Germain D. (2016). Late-glacial and Holocene evolution as a driver of diversity
886and complexity of the northeastern North American alpine landscapes: a synthesis. *Canadian Journal*
887*of Earth Sciences* **53**, 494-505.

888 McKenzie D., Jackson J. & Priestley K. (2005). Thermal structure of oceanic and continental
889lithosphere. *Earth and Planetary Science Letters* **233**, 337-349.

890 Messiga B. & Bettini E. (1990). Reactions behaviour during kelyphite and symplectite formation:
891a case study of mafic granulites and eclogites from the Bohemian Massif. *European Journal of*
892*Mineralogy* **2**, 125-144.

893 Nicollet C., Leyreloup A. & Dupuy C. (1979). Petrogenesis of High Pressure Trondhjemitic
894Layers in Eclogites and Amphibolites from Southern Massif Central, France. *in Trondhjemites,*
895*Dacites, and Related Rocks*, Ed: Barker, F. (Ed.) **6**, 435-463.

896 O'Beirne-Ryan A. M., Jamieson R. A. & Gagnon Y. D. (1990). Petrology of garnet–
897clinopyroxene amphibolites from Mont Albert, Gaspé, Quebec. *Canadian Journal of Earth Sciences*
898**27**, 72-86.

899 Olejczyk P. & Gray J. T. (2007). The relative influence of Laurentide and local ice sheets during
900the last glacial maximum in the eastern Chic-Chocs Range, northern Gaspé Peninsula, Quebec.
901*Canadian Journal of Earth Sciences* **44**, 1603-1625.

902 Operta M., Pamić J., Balen D. & Tropper P. (2003). Corundum-bearing amphibolites from the
903metamorphic basement of the Krivaja--Konjuh ultramafic massif (Dinaride Ophiolite Zone, Bosnia).
904*Mineralogy and Petrology* **77**, 287-295.

905 Palin R. M., St-Onge M. R., Waters D. J., Searle M. P., Dyck B. (2014). Phase equilibria
906modelling of retrograde amphibole and clinozoisite in mafic eclogite from the Tso Morari massif,
907northwest India: constraining the P–T–M(H_2O) conditions of exhumation. *Journal of Metamorphic*
908*Geology* **32**, 675-693.

909 Palin R. M., White R. W., Green E. C. R., Diener J. F. A., Powell R. & Holland T. J. B. (2016).
910High-grade metamorphism and partial melting of mafic and intermediate rocks. *Journal of*
911*Metamorphic Geology* **34**, 871-892.

912 Pincivy A., Malo M., Ruffet G., Tremblay A. & Sacks P. (2003). Regional metamorphism of the
913Appalachian Humber zone of Gaspé Peninsula: $^{40}Ar/^{39}Ar$ evidence for crustal thickening during the
914Taconian Orogeny. *Canadian Journal of Earth Sciences* **40**, 2, 301-315.

915 Pinet N. & Tremblay A. (1995). Tectonic evolution of the Quebec-Maine Appalachians: from
916oceanic spreading to obduction and collision in the Northern Appalachians. *American Journal of*
917*Science* **295**, 2, 173-200.

918 Plank T., Cooper L. B. & Manning C. E. (2009). Emerging geothermometers for estimating slab
919surface temperatures. *Nature Geoscience* **2**, 611-615.

920 Plunder A., Agard P., Chopin C., Soret M., Okay A. I. & Whitechurch H. (2016). Metamorphic
921sole formation, emplacement and blueschist facies overprint: early subduction dynamics witnessed by
922western Turkey ophiolites. *Terra Nova* **28**, 329-339.

923 Powell R. (1985). Regression diagnostics and robust regression in geothermometer/geobarometer
924calibration: the garnet-clinopyroxene geothermometer revisited. *Journal of Metamorphic Geology* **3**,
925231-243.

926 Pratt J. H. (1906). Corundum and its occurrence and distribution in the United States (a revised
927and enlarged edition of Bulletin 180). *USGS Numbered Series* 269, 175 p.,
928https://pubs.er.usgs.gov/publication/b269

929 Prigent C., Agard P., Guillot S., Godard M. & Dubacq B. (2019). Mantle Wedge (De)formation
930During Subduction Infancy: Evidence from the Base of the Semail Ophiolitic Mantle. *Journal of*
931*Petrology* **59**, 11, 2061-2092.

932 Prigent C., Guillot S., Agard P., Lemarchand D., Soret M., & Ulrich M. (2018). Transfer of
933subduction fluids into the deforming mantle wedge during nascent subduction: Evidence from trace
934elements and boron isotopes (Semail ophiolite, Oman). *Earth and Planetary Science Letters* **484**, 213-
935228.

936 Rioux M., Garber J., Bauer A., Bowring S., Searle M., Kelemen P. & Hacker B. (2016).
937Synchronous formation of the metamorphic sole and igneous crust of the Semail ophiolite: New
938constraints on the tectonic evolution during ophiolite formation from high-precision U-Pb zircon
939geochronology. *Earth Planetary Science Letters* **451**, 185-195.

940 Schiffman P. & Staudigel H. (1995). The smectite to chlorite transition in a fossil seamount
941hydrothermal system: the Basement Complex of La Palma, Canary Islands. *Journal of Metamorphic*
942*Geology* **13**, 487-498.

943 Schmidt M. W. & Poli S. (2004). Magmatic Epidote. *Reviews in Mineralogy and Geochemistry*,
944Mineralogical Society of America **56**, 399-430.

945 Searle M. & Cox J. (1999). Tectonic setting, origin, and obduction of the Oman ophiolite.
946*Geological Society of America Bulletin* **111**, 104-122.

947 Searle M. & Malpas J. (1982). Petrochemistry and origin of sub-ophiolitic metamorphic and
948related rocks in the Oman Mountains. *Journal of the Geological Society, Geological Society of*
949*London* **139**, 235-248.

950 Searle M., Waters D., Garber J., Rioux M., Cherry A. & Ambrose T. (2015). Structure and
951metamorphism beneath the obducting Oman ophiolite: Evidence from the Bani Hamid granulites,
952northern Oman mountains. *Geosphere* **11**, 1812-1836.

953 Sirois L. & Grandtner M. (1992). A phyto-ecological investigation of the Mount Albert
954serpentine plateau. in *The Ecology of Areas with Serpentinized Rocks: A World View*, Springer
955Netherlands Eds., 115-133.

956 Skelton A., Arghe F. & Pitcairn I. (2010). Regional mapping of pre-metamorphic spilitization and
957associated chemical mobility in greenschist-facies metabasalts of the SW Scottish Highlands. *Journal*
958*of the Geological Society* **167**, 5, 1049-1061.

959 Soret M., Agard P., Dubacq B., Plunder A. & Yamato P. (2017). Petrological evidence for
960stepwise accretion of metamorphic soles during subduction infancy (Semail ophiolite, Oman and
961UAE). *Journal of Metamorphic Geology* **35**, 1051-1080.

962 Soret M., Agard P., Dubacq B., Vitale-Brovarone A., Monié P., Chauvet A., Whitechurch H. &
963Villemant, B. (2016). Strain localization and fluid infiltration in the mantle wedge during subduction
964initiation: Evidence from the base of the New Caledonia ophiolite. *Lithos* **244**, 1-19.

965 Spear F. (1993). Metamorphic Phase Equilibria and Pressure-Temperature-Time Paths
966*Mineralogical Society of America*, WashinGrton, D. C, 799 p.

967 Spray, J. G. (1984). Possible causes and consequences of upper mantle decoupling and ophiolite
968displacement. *Geological Society, London, Special Publications* **13**, 255-268.

969 Spray J. G., Bebien J., Rex D. C. & Roddick J. C. (1984). Age constraints on the igneous and
970metamorphic evolution of the Hellenic-Dinaric ophiolites. *Geological Society of London, Special*
971*Publication*s **17**, 619-627.

972 Suhr G. & Cawood P. A. (1993). Structural history of ophiolite obduction, Bay of Islands,
973Newfoundland. *Geological Society of America Bulletin* **105**, 399-410.

974 Tremblay A. & Pinet N. (2016). Late Neoproterozoic to Permian tectonic evolution of the Quebec
975Appalachians, Canada. *Earth Science Reviews* **160**, 131-170.

976 Tremblay A., Ruffet G. & Bédard J. H. (2011). Obduction of Tethyan-type ophiolites - A case-
977study from the Thetford-Mines ophiolitic Complex, Quebec Appalachians, Canada. *Lithos* **125**, 10-26

978 Tropper P. & Recheis A. (2003). Garnet zoning as a window into the metamorphic evolution of a
979crystalline complex: the northern and central Austroalpine Ötztal-Complex as a polymorphic example.
980*Mitteilungen der Österreichischen Geologischen Gesellschaft* **94**, 27-53.

981 Trzcienski W. E. (1988). Retrograde eclogite from Mont Albert, Gaspé, Quebec. *Canadian*
982*Journal of Earth Sciences* **25**, 30-37.

983 Trzcienski W. E., Gromet L. P. & Kinny P. (1995). Comparative conventional, Kober, and
984SHRIMP II analyses of zircons from within the Mont Albert, Gaspé, Québec, Canada Ultramafic
985Complex. *Geological Society of America, Annual Meeting, New Orleans* **27** (A 436).

986 Vaughan A. P. & Scarrow J. H. (2003). Ophiolite obduction pulses as a proxy indicator of
987superplume events? *Earth and Planetary Science Letters* **213**, 407-416.

988 Vidal O., De Andrade V., Lewin E., Munoz M., Parra T. & Pascarelli S. (2006). P-T-
989deformation-Fe^{3+}/Fe^{2+} mapping at the thin section scale and comparison with XANES mapping:
990application to a garnet-bearing metapelite from the Sambagawa metamorphic belt (Japan). *Journal of*
991*Metamorphic Geology* **24**, 669-683.

992 Wakabayashi J. (1990). Counterclockwise P-T-t Paths from Amphibolites, Franciscan Complex,
993California: Relics from the Early Stages of Subduction Zone Metamorphism. *The Journal of Geology*
994**98**, 657-680.

995 Wakabayashi J. & Dilek Y. (2000). Spatial and temporal relationships between ophiolites and
996their metamorphic soles: A test of models of forearc ophiolite genesis. *Geological Society of America*
997*Special Papers* **349**, 53-64.

998 Wakabayashi J. & Dilek Y. (2003). What constitutes “emplacement” of an ophiolite?:
999Mechanisms and relationship to subduction initiation and formation of metamorphic soles. *Geological*
1000*Society of London Special Publications* **218**, 427-447.

1001 Williams H. & Grant A. C. (1998). Tectonic Assemblages Map, Atlantic Region, Canada.
1002*Geological Survey of Canada* Open File 3657.

1003 White R. W., Powell R., Holland T. J. B., Johnson T. E. & Green E. C. R. (2014a). New mineral
1004activity-composition relations for thermodynamic calculations in metapelitic systems. *Journal of*
1005*Metamorphic Geology* **32**, 261-286.

1006 White R. W., Powell R. & Johnson T. E. (2014b). The effect of Mn on mineral stability in
1007metapelites revisited: new a-x relations for manganese-bearing minerals. *Journal of Metamorphic*
1008*Geology* **32**, 809-828.

1009 White R. W., Powell R., Holland T. J. B. and Worley A. (2000). The effect of TiO_2 and Fe_2O_3 on
1010metapelitic assemblages at greenschist and amphibolite facies conditions: mineral equilibria
1011calculations in the system K_2O–FeO–MgO–Al_2O_3–SiO_2–H_2O–TiO_2–Fe_2O_3. *Journal of Metamorphic*
1012*Geology* **18**, 497-511.

1013 Whitehead J., Reynolds P. H. & Spray J. G. (1995). The sub-ophiolitic metamorphic rocks of the
1014Québec Appalachians. *Journal of Geodynamics* **19**, 325-350.

1015 Whitney D. L. & Evans B. W. (2010). Abbreviations for names of rock-forming minerals.
1016*American Mineralogist* **95**, 185-187.

1017 Williams H. (1979). Appalachian Orogen in Canada. *Canadian Journal of Earth Sciences* **16**,
1018792-807.

1019 Williams H. & Smyth W. R. (1973). Metamorphic aureoles beneath ophiolite suites and alpine
1020peridotites: tectonic implications with west Newfoundland examples. *American Journal of Science*
1021**273**, 594-621.

1022 Wolf M. B. & Wyllie P. J. (1994). Dehydration-melting of amphibolite at 10 kbar: the effects of
1023temperature and time. *Contributions to Mineralogy and Petrology* **115**, 369-383.

1024 Wu C. M. (2015). Revised empirical garnet-biotite-muscovite-plagioclase geobarometer in
1025metapelites. *Journal of Metamorphic Geology* **33**, 167-176.

1026 Wu C. M. & Chen H.-X. (2015). Calibration of a Ti-in-muscovite geothermometer for ilmenite-
1027and Al_2SiO_5-bearing metapelites. *Lithos* **212-215**, 122-127.

1028 Wu C. M. & Zhao G. (2006). Recalibration of the Garnet–Muscovite (GM) Geothermometer and
1029the Garnet–Muscovite–Plagioclase–Quartz (GMPQ) Geobarometer for Metapelitic Assemblages.
1030*Journal of Petrology* **47**, 2357-2368.

1031 Wu C. M. & Zhao G. C. (2007). The metapelitic garnet-biotite-muscovite-aluminosilicate-quartz
1032(GBMAQ) geobarometer. *Lithos* **97**, 365-372.

1033

FIGURE CAPTIONS

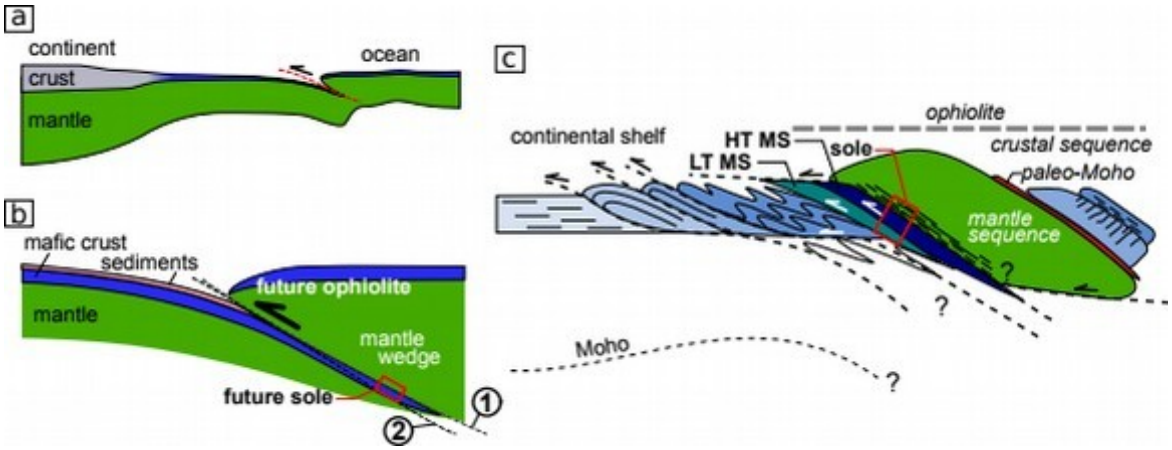

Figure 1: Schematic cross-sections showing the general geodynamic setting and its evolution during subduction infancy and ophiolite obduction, with emphasis on the ophiolitic sole. Redrawn after Agard et al. (2016) and Searle et al. (2015). (a) Intra-oceanic subduction initiation, prior to ophiolite obduction. (b) Close-up view on the formation and accretion of the metamorphic sole to the mantle wedge. Accretion of crustal-derived material implies displacement of the subduction interface from thrust 1 to thrust 2. (c) Obduction of the ophiolite and its sole (red rectangle). The sole has an apparent inverted metamorphic gradient and includes, from bottom to top: greenschist- and lower amphibolite facies metamorphic rocks (LT MS: low temperature metamorphic sole), higher amphibole to granulite facies metamorphic rocks (HT MS: high temperature), and peridotite of mantle origin showing multiple deformation events (from ~1200°C to ~650°C: Linkens et al., 2011 ; Prigent et al., 2018). The Mont Albert ophiolitic complex lacks the crustal sequence.

1048

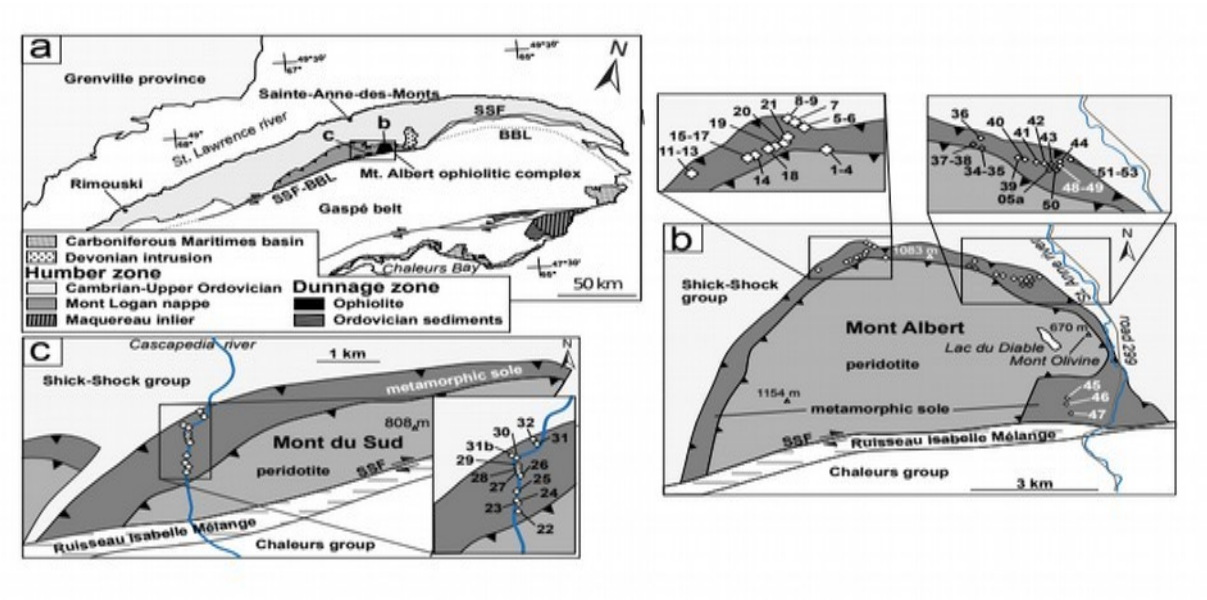

1049Figure 2: Geological maps of the Mont Albert ophiolitic complex and sample location. (a) Simplified
1050geological map of the Gaspé peninsula (modified after Malo et al., 2008 and Williams and Grant,
10511998). The Mont Albert ophiolitic complex is indicated by the central rectangle. (b) Simplified
1052geological map of the Mont Albert area (after MacGregor and Basu, 1979; Gagnon and Jamieson,
10531986). Numbers indicate sample location, as shown in insets for readability. (c) Geological map of the
1054Mont du Sud area (after the geological map available from SIGEOM http://sigeom.mines.gouv.qc.ca).
1055Sampling of the metamorphic sole was focused on the shore of the Cascapedia River. SSF: South
1056Schick-Schock Fault; BBL: Baie Verte-Brompton Line.

1057

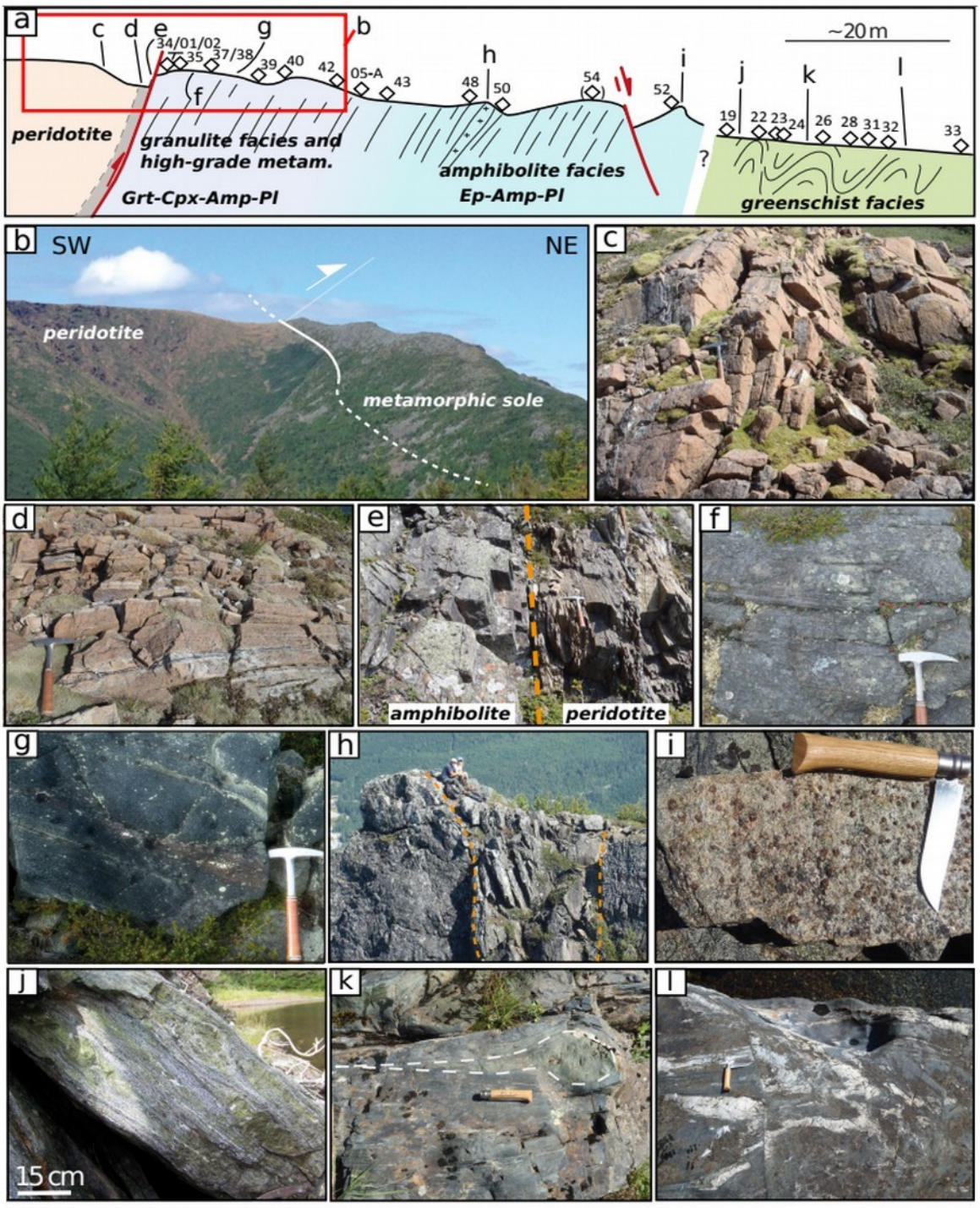

1059Figure 3: Representative geology of the base of the Mont Albert ophiolitic complex. (a) Schematic
1060cross-section, indicating the position of samples presented in this study (diamonds and numbers) and
1061the position of fields photographs underneath (letters). (b) Large-scale view from the summit of Mont
1062Olivine of the north-east ridge of Mont Albert, with peridotite on the left (brass colour) and

amphibolite on the right (dark grey). The contact is partly hidden by vegetation and grey boulders (dotted line). (c) Typical aspect of the peridotite away from the contact. (d) Serpentinite unit at the base of the peridotite, with oxide-rich layers, north-east of the summit of Mont Albert. (e) The peridotite / amphibolite contact as found on top of Mont Albert. (f) Typical aspect of the high-grade garnet-clinopyroxene amphibolite. (g) Garnet-rich layer (left of hammer head) alternating with albite-epidote rich layers (top of image) in the high-grade amphibolite. (h) View of a 'sill' (bounded by orange dashes) along the north-east arête of Mont Albert, with quartz-plagioclase-hornblende in the centre and quartz-mica-gedrite on the margins (samples MA-14-48-49 on Fig. 2b and 6j). Foliation is subparallel to the intrusion. (i) Garnet-bearing metapelites along the 'Marches du Géant' normal fault system, ≥ 40 m away from the contact with the peridotite (near sample MA-14-50, Fig. 2b, 6a). (j), (k) and (l) are typical outcrops of the low-grade amphibolite. Deformation is highlighted by quartz-albite-epidote assemblages found in shear zones, as layers, veinlets and around deformed pillows (highlighted in k). (j): west of summit of Mont Albert, near sample MA-14-19 (Fig. 2b and 5c). (k): south of Mont Albert (near sample MA-14-46, Fig. 2b). (l) south-west of Mont du Sud near sample MA-14-24 (Fig. 2c).

1079

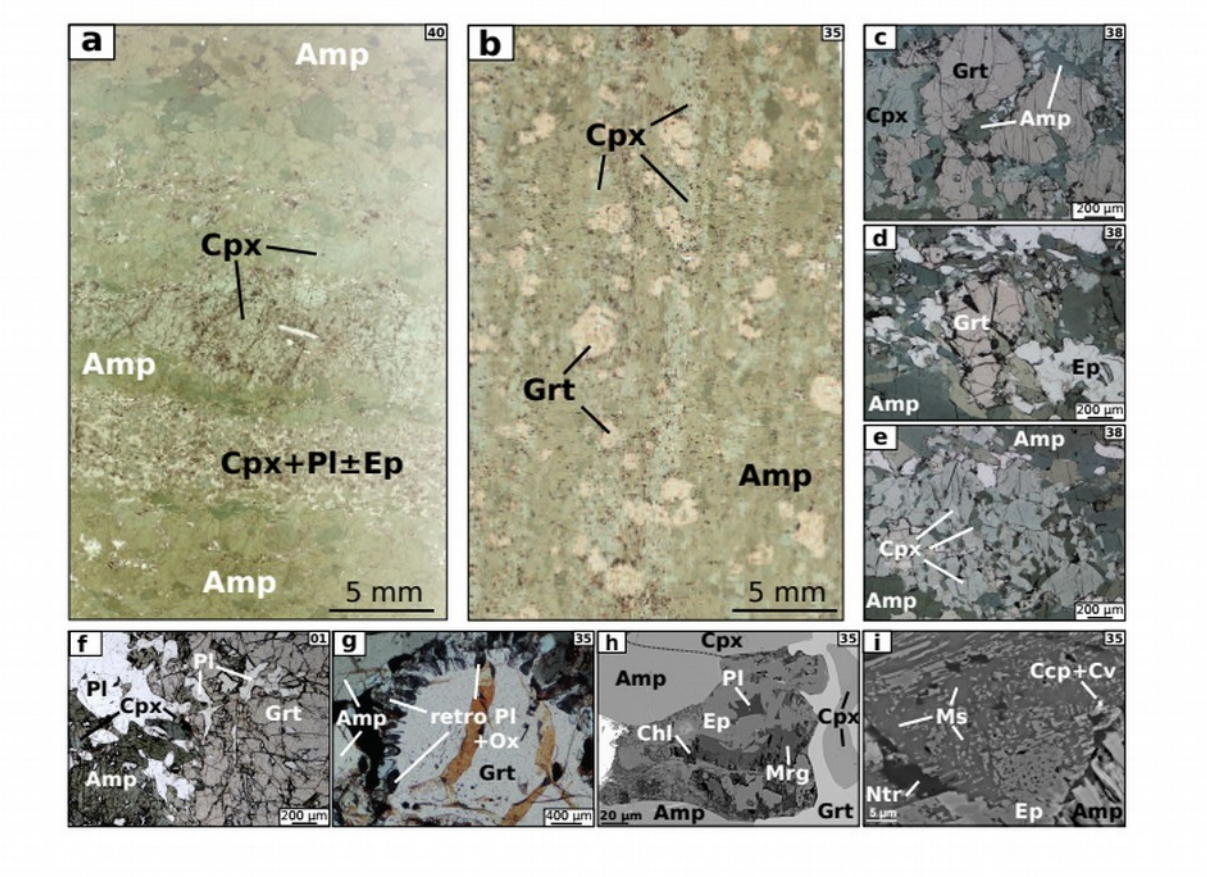

1080Figure 4: Typical aspect of high-grade amphibolite, with thin sections scans, microphotographs and
1081SEM images. (a) Clinopyroxene-rich amphibolite, without garnet. Foliation is roughly horizontal.
1082Amphibole varies from deep to paler green. Clinopyroxene (pale green, paler than amphibole) is often
1083found forming layers where large, fractured and deformed clinopyroxene crystals are surrounded by
1084smaller clinopyroxene crystals and plagioclase (translucent). (b) Garnet-clinopyroxene-epidote
1085amphibolite. Foliation is subvertical. (c-d-e) close-up microphotographs of sample MA-14-38,
1086showing ~500 µm anhedral garnet crystals and aggregated smaller (100-200 µm) euhedral garnet
1087crystals, both often with symplectitic rim (e). Epidote is a crystallisation product in the simplectite.
1088Clinopyroxene is found as ≥1mm crystals and as ~100µm crystals growing with amphibole. (e)
1089Clinopyroxene-amphibole symplectite. (f) Plagioclase-garnet-amphibole symplectite with minor
1090clinopyroxene. (g): sample MA-14-35; garnet rims with symplectite texture, retrogressed plagioclase
1091and Fe-Ti oxides. (h-i) close-up views of phases associated with retrogressed plagioclase within the
1092symplectite (note the texture of garnet, see also Fig. 7c). Plagioclase is preserved associated to epidote,

and replaced by very fine epidote-muscovite intergrowths. Margarite, chlorite, sulfides and natrolite appear as later alteration products.

1096

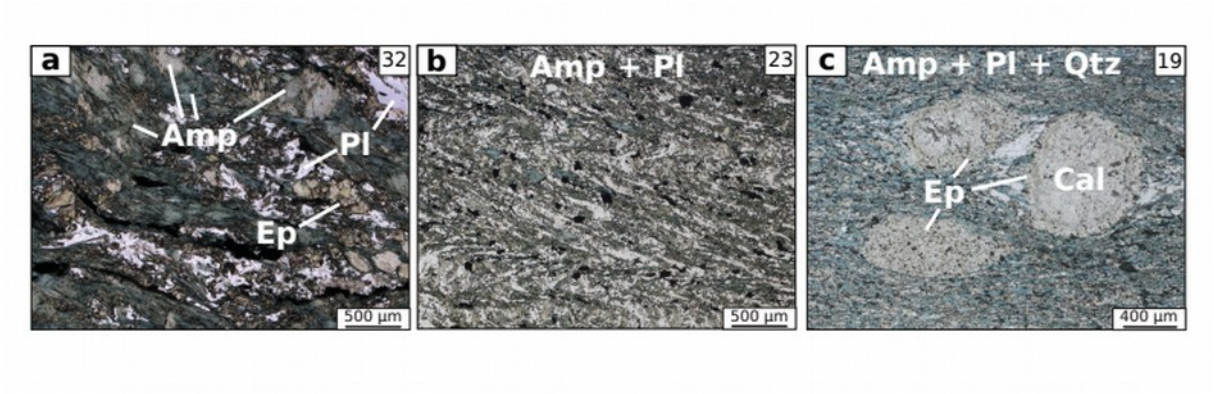

1097Figure 5: Selected thin section microphotographs of the low-grade amphibolite. (a) Plagioclase-
1098epidote amphibolite where amphibole shows pale green cores and darker blue-green rims. (b) Incipient
1099crenulation cleavage in schistose amphibolite, as typically found along the Cascapedia river. (c)
1100Calcite-epidote filled spherulites in amphibolite, with quartz and albite. Foliation is horizontal.

1101

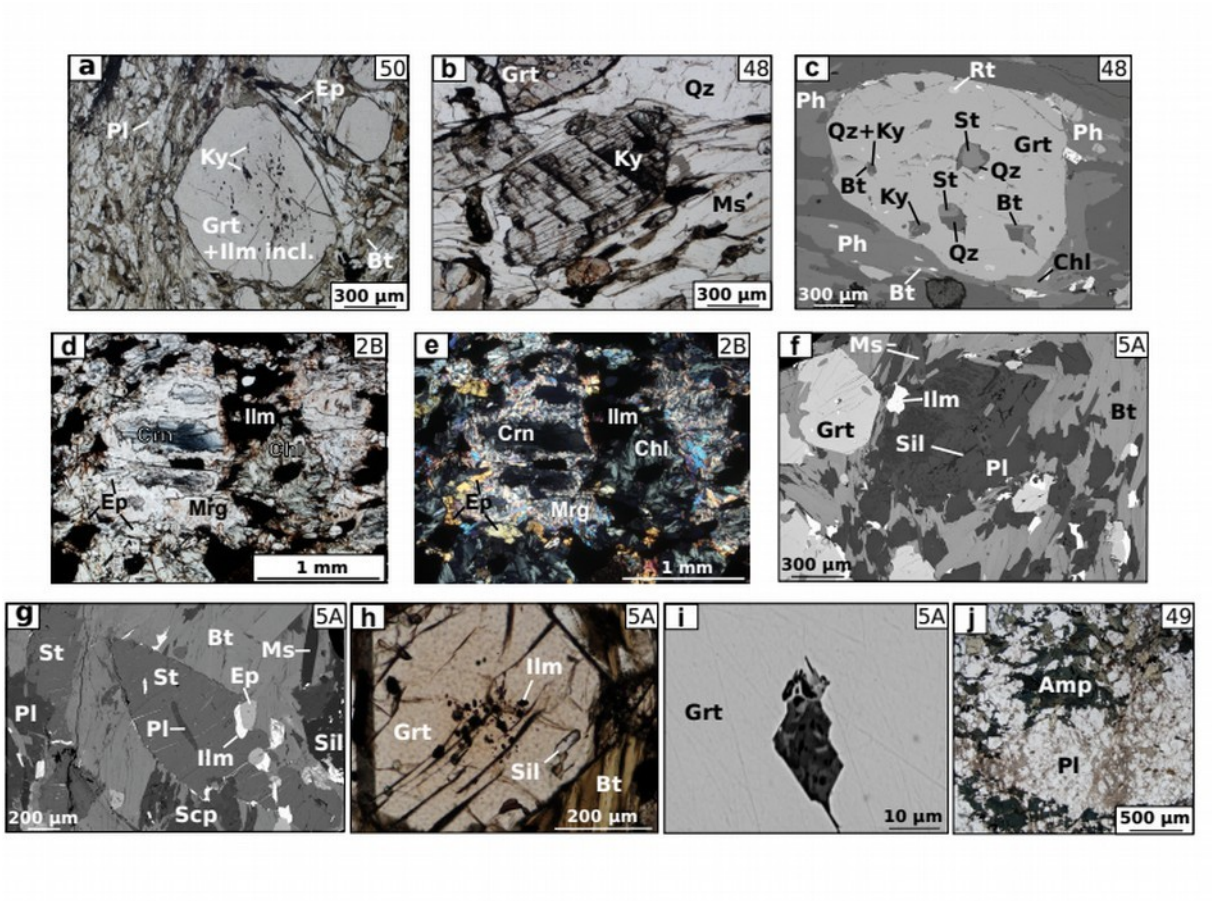

Figure 6: Representative mineralogy of metapelites and associated rocks found in the metamorphic sole of Mont Albert. (a) Garnet-kyanite-biotite-plagioclase metapelite (see Fig. 3i). (b) Kyanite is found as a porphyroclast and included in garnet (SEM image c). Garnet also includes staurolite, biotite, quartz and rutile (c). (d – plane-polarized light) and (e – crossed polars) show microphotographs of corundum-epidote-ilmenite assemblage in red oxide-rich layers, retrogressed to margarite, chlorite, paragonite and diaspore (both too small to show on micrograph). (f-g-h-i) SEM images and microphotographs of sample MA-15-05A, found ~20 m away from the peridotite. Sillimanite is observed as abundant needles in plagioclase (f) and in prismatic form associated with scapolite and staurolite (g). These are both in the foliation and cross-cutting the foliation as in (g). (h) and (i) show inclusions in garnet from biotite-rich layers, with oxides in the core and sillimanite in the rim. SEM revealed that some inclusions have negative crystal shape and contain polycrystalline silicates (too small for determination) together with apparent porosity. (j) Texture of the retrogressed sill with millimetre-scale plagioclase and amphibole.

1116

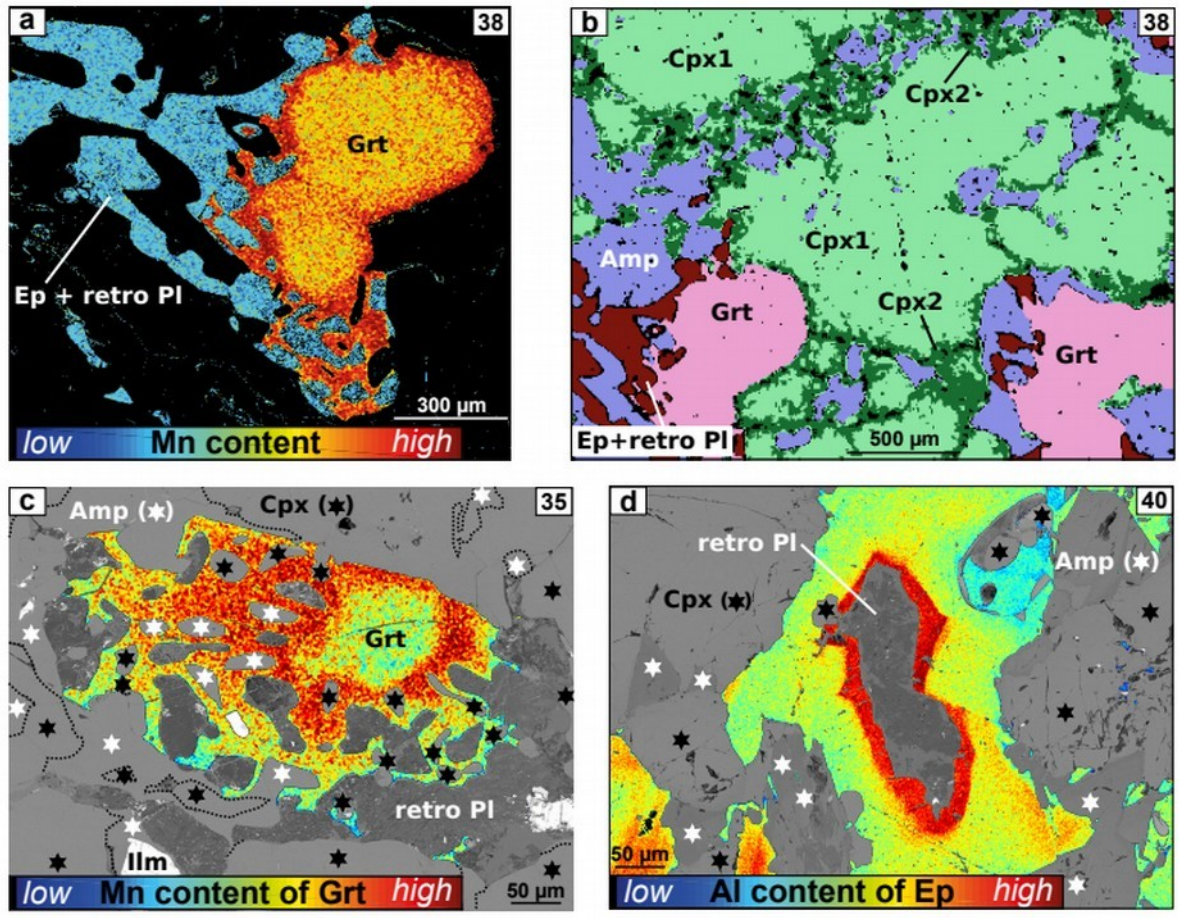

1118Figure 7: Texture and composition of minerals associated with the garnet-amphibole-clinopyroxene
1119symplectite. (a) and (b) Mineral assemblage and Mn content in sample MA-14-38. The symplectic
1120garnet rim has high Mn, and is intimately associated to retrogressed plagioclase and epidote. Two
1121generations of clinopyroxene are unambiguously evidenced from their Al content (see corresponding
1122compositions in Fig. 8d). (c) Mn content of garnet over SEM image of texture of symplectite in
1123sample MA-14-35. Garnet is associated with amphibole, clinopyroxene, oxide and retrogressed
1124plagioclase (labelled “retro Pl”). Clinopyroxene and amphibole, hard to distinguish on SEM images,
1125are labelled with black and white stars respectively, and contoured with dotted lines. (d) Al content of
1126epidote over SEM image of epidote crystallised around retrogressed plagioclase. Clinopyroxene and
1127amphibole are intergrown on each side of the image and labelled as in (c).
1128

1129

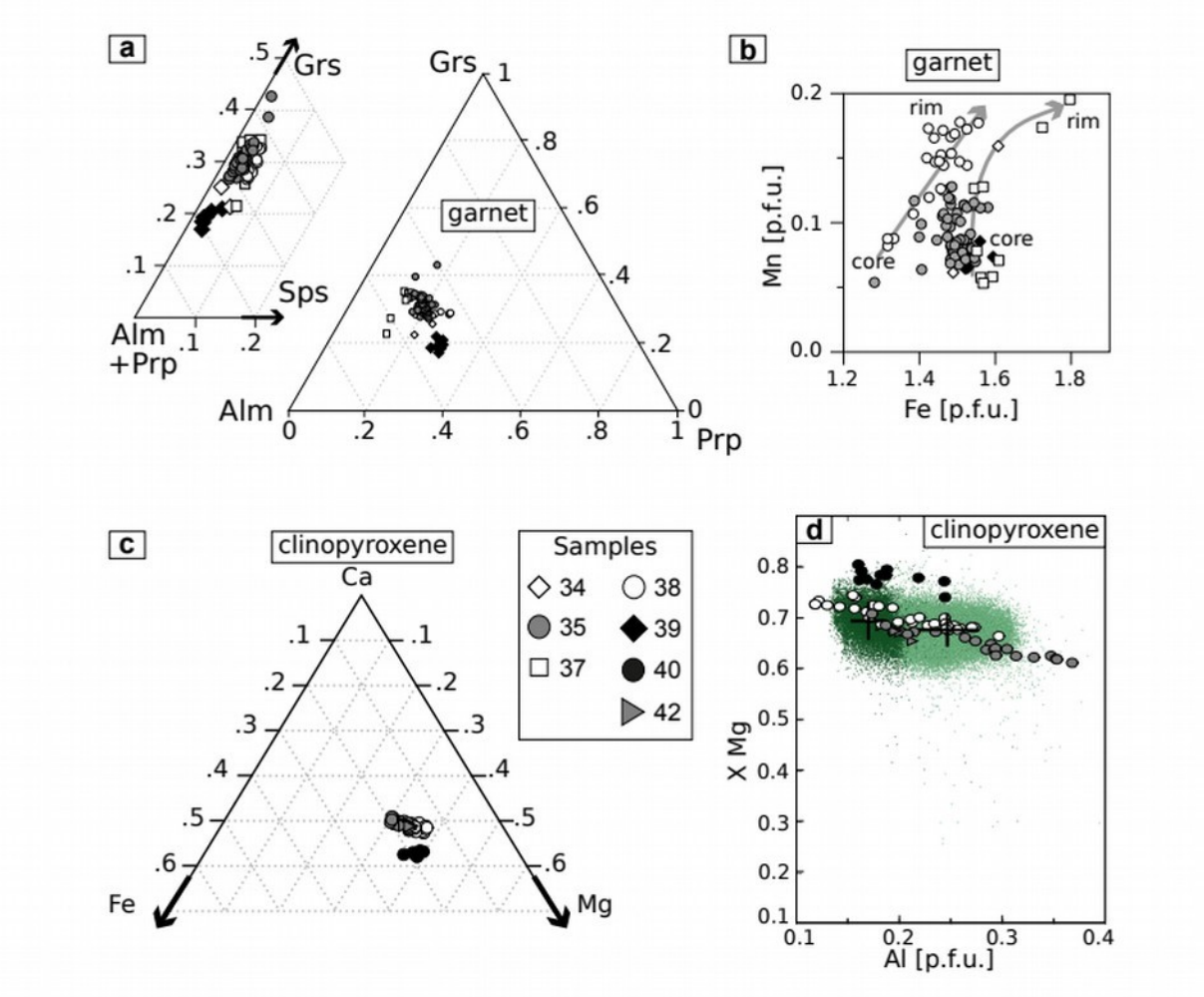

1130Figure 8: composition of garnet and clinopyroxene from the mafic rocks. (a) and (b) show garnet
1131composition, plotted with and without the spessartine component in (b). Arrows in (b) emphasize the
1132increase in Mn in the symplectite rimming garnet cores (see also Fig. 7a-c), mostly at the expense of
1133Fe. (c) and (d) show clinopyroxene composition, from point EPMA measurements as circles and from
1134EPMA mapping as small dots coloured according to their Al content, corresponding to CPX1 (Al-rich
1135cores) and CPX2 (Al-poor rims) in Fig. 7b (sample MA-14-38). Crosses in (d) indicate average
1136composition and 2-sigma standard deviation of each clinopyroxene generation measured on the area of
1137Fig. 7b.

1138

1139

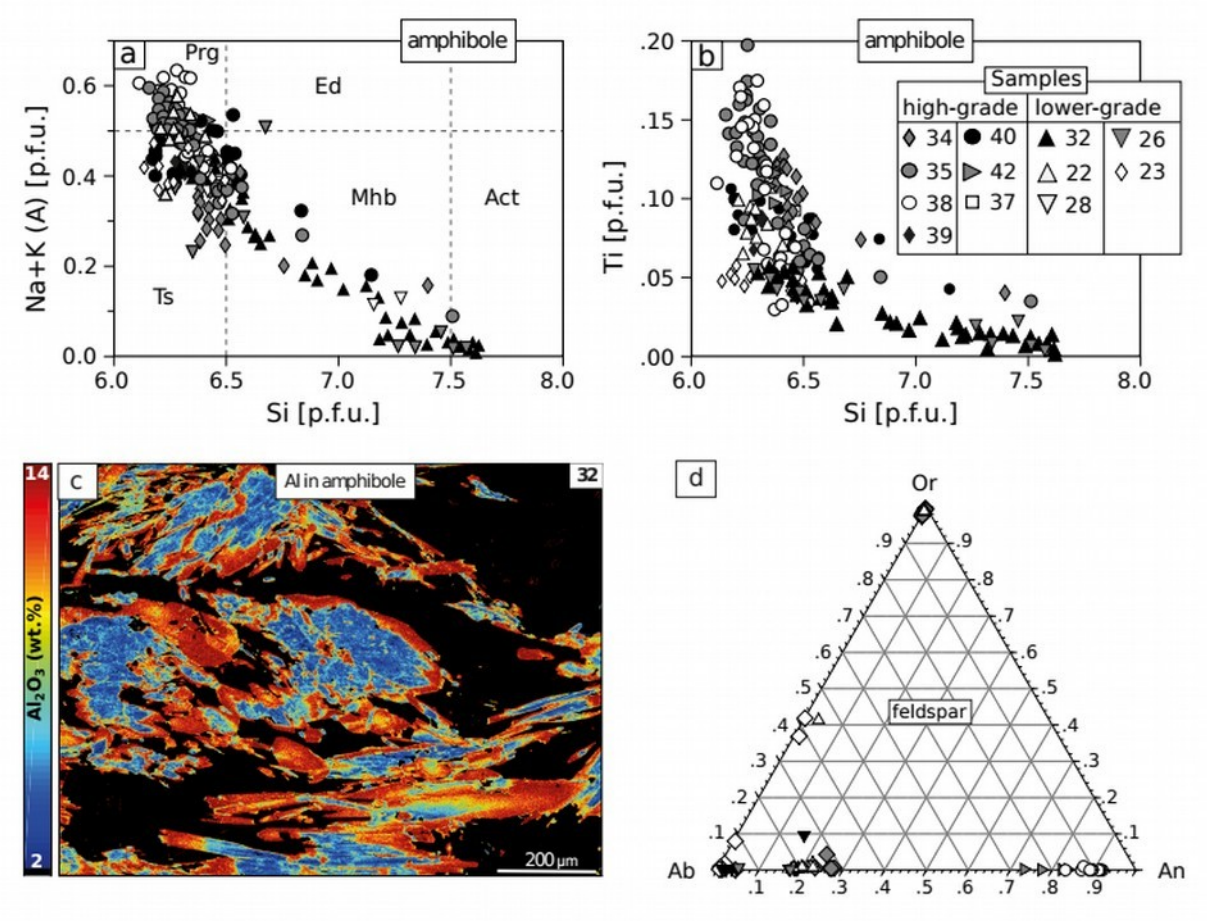

1140Figure 9: Composition of amphibole and feldspar in high-grade and lower-grade mafic rocks of the
1141metamorphic sole of Mont Albert. (a) Alkali content of the A site of amphibole versus Si content,
1142linked to Ti content (b). Samples close to the contact with the peridotite have highest alkali and Ti. (c)
1143Al content of amphibole in sample MA-14-32 (top of lower-grade unit along the Cascapedia river)
1144showing actinolite-rich cores and pargasite-rich rims, measured with SEM. Numbers on the left-hand
1145side colour scale indicate concentration as obtained from EPMA point analysis. (d) Composition of
1146feldspar.

1147

1148

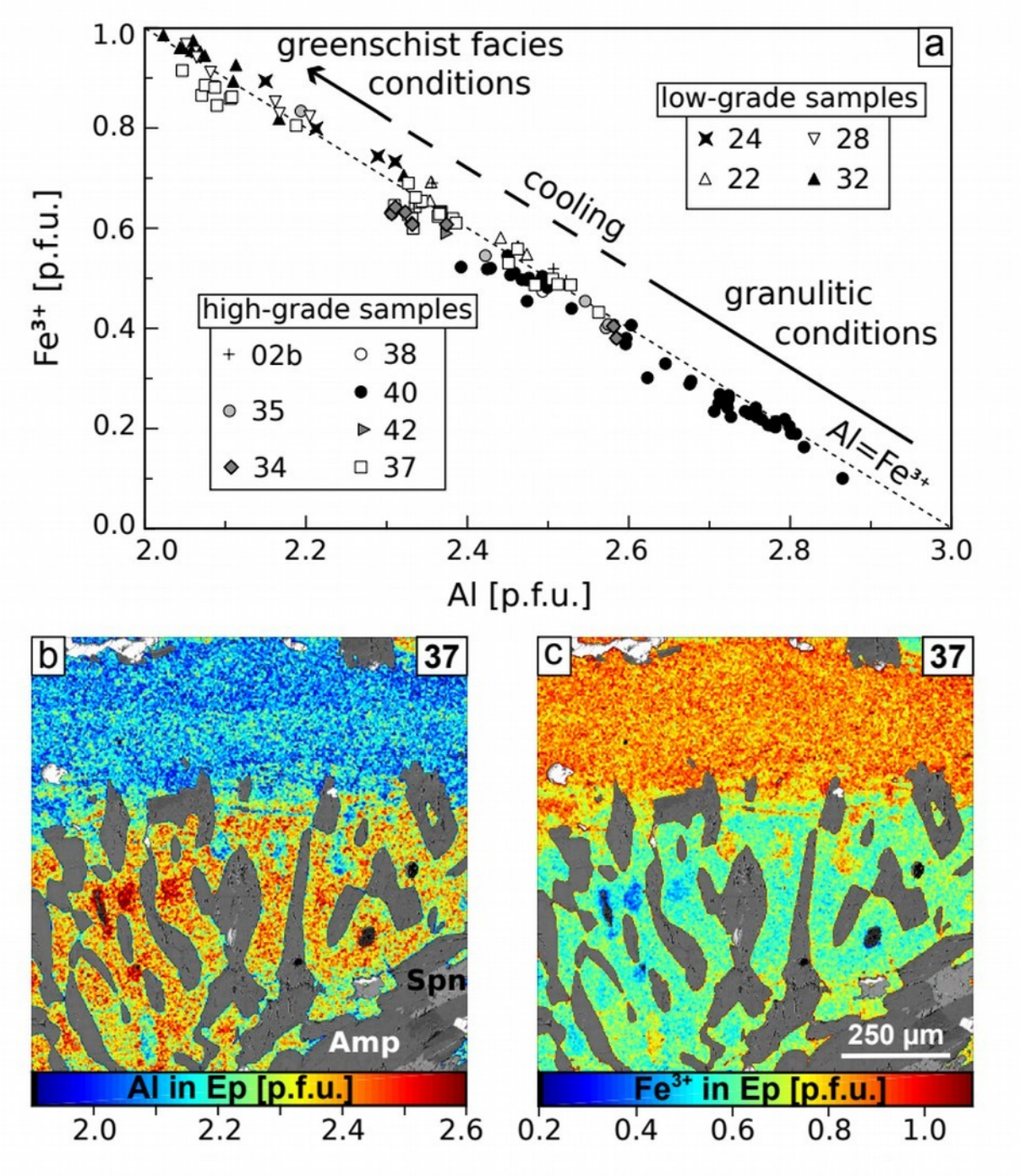

1149Figure 10: Composition of epidote in high-grade and lower-grade mafic rocks of the metamorphic sole
1150of Mont Albert. (a) Compilation of analyses showing Fe^{3+} content versus Al content. (b) and (c) show
1151map views of Al and Fe^{3+} content of epidote in sample MA-14-37, laid over a back-scattered electron
1152EPMA image of an amphibole-epidote symplectite cross-cut by an epidote vein (horizontal, on top).

Fe^{3+}-rich epidote is found in the vein, Al-rich epidote in the symplectite, with the cores of symplectite crystals being richest in Al.

1155

1156

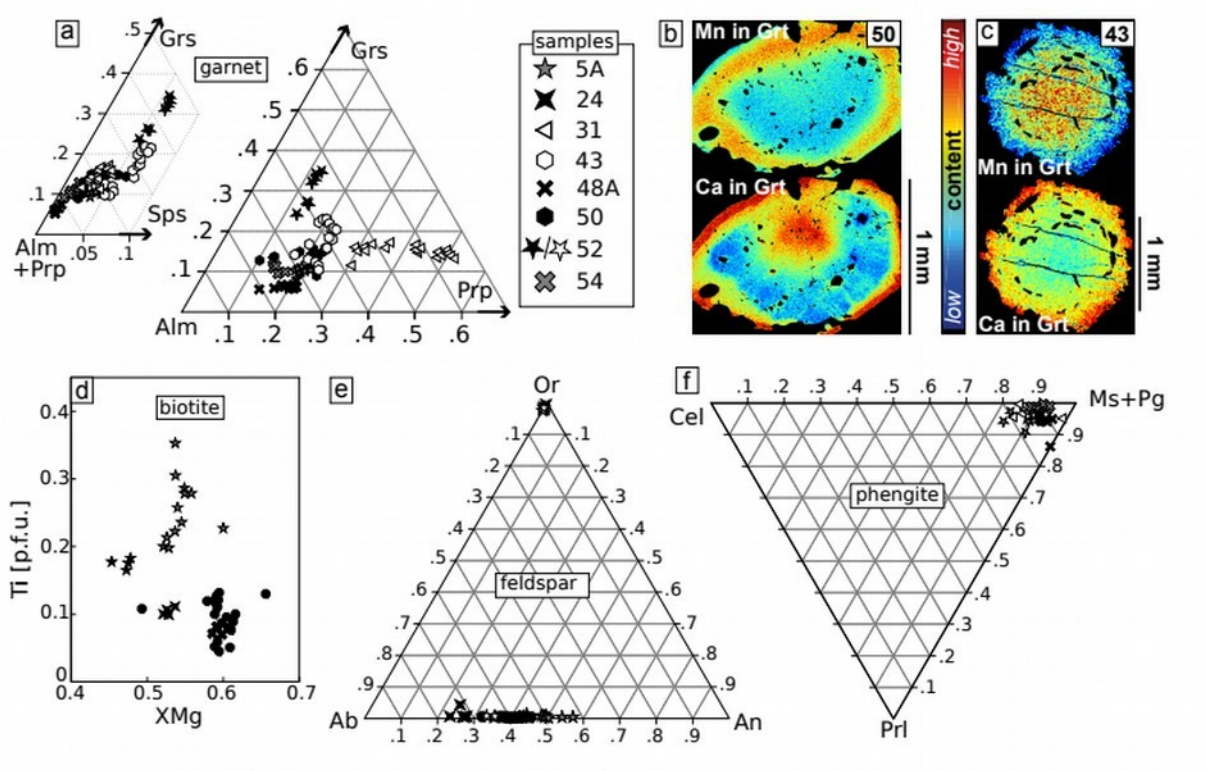

1157Figure 11: Composition of minerals in metasediments from the metamorphic sole of the Mont Albert
1158complex. (a) Garnet composition, plotted with and without the spessartine component. Zoning in
1159garnet is shown as measured with SEM for Ca and Mn in high-grade samples in (b) and (c), all scaled
1160on the colourbar in b. (d) Ti content versus Xmg of biotite. (e) Composition of feldspar. (f)
1161Composition of phengite.

1162

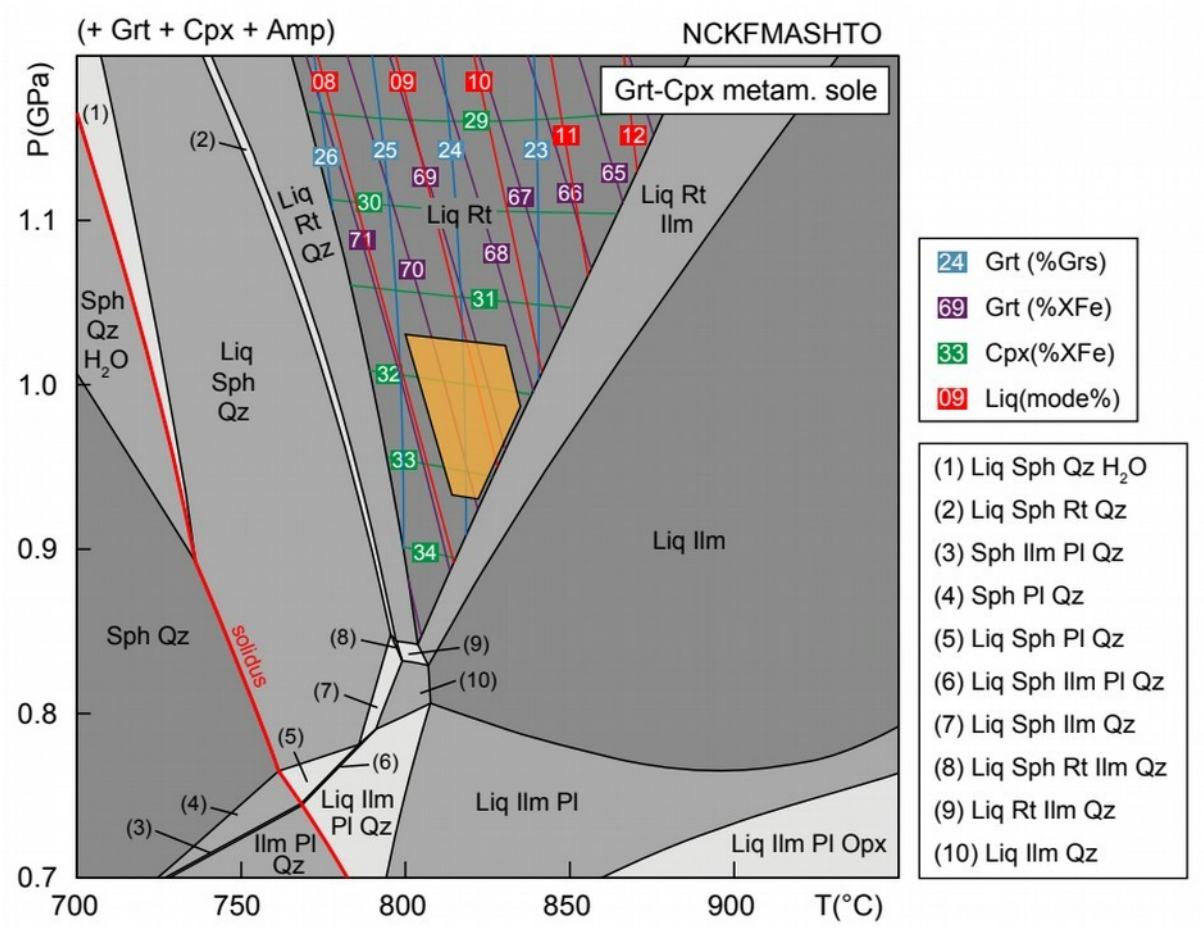

1164Figure 12: pressure-temperature pseudosection in NCKFMASHTO for a mafic rock representative of 1165the garnet-bearing high-grade unit. Garnet, clinopyroxene and amphibole are present throughout the 1166pseudosection. The solidus is drawn with a red line and isopleths are shown for garnet, clinopyroxene 1167and melt fraction as discussed in the text. The orange field highlights pressure-temperature conditions 1168matching the petrography.

1169

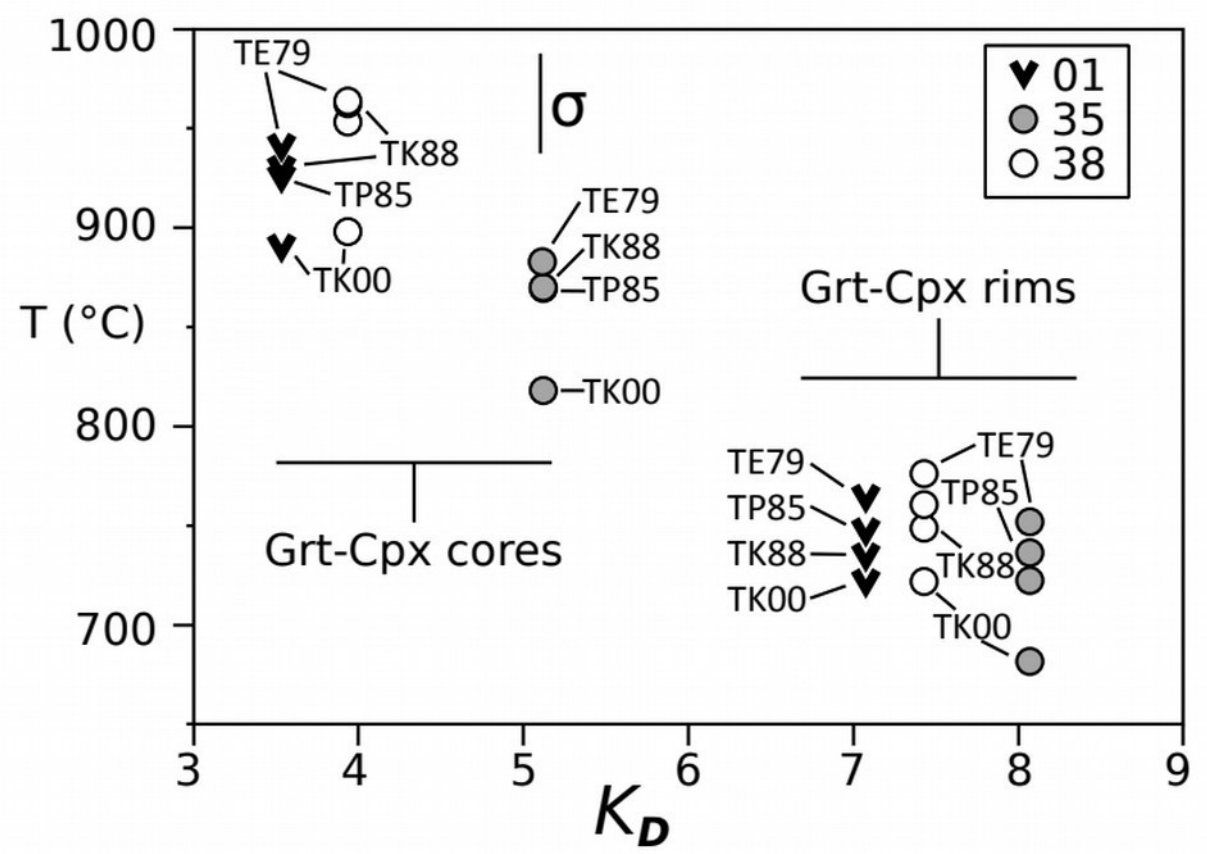

1171Figure 13: Results of garnet-clinopyroxene thermometry, calculated at fixed pressure of 0.95 GPa 1172using the calibrations of Ellis and Green (1979, TE79), Powell (1985, TP85), Krogh Ravna (1988, 1173TK88 ; 2000, TK00). Uncertainties on temperature estimates are consistently of the order of 50°C, 1174including ~10°C uncertainty originating from pressure estimates.

1175

1176

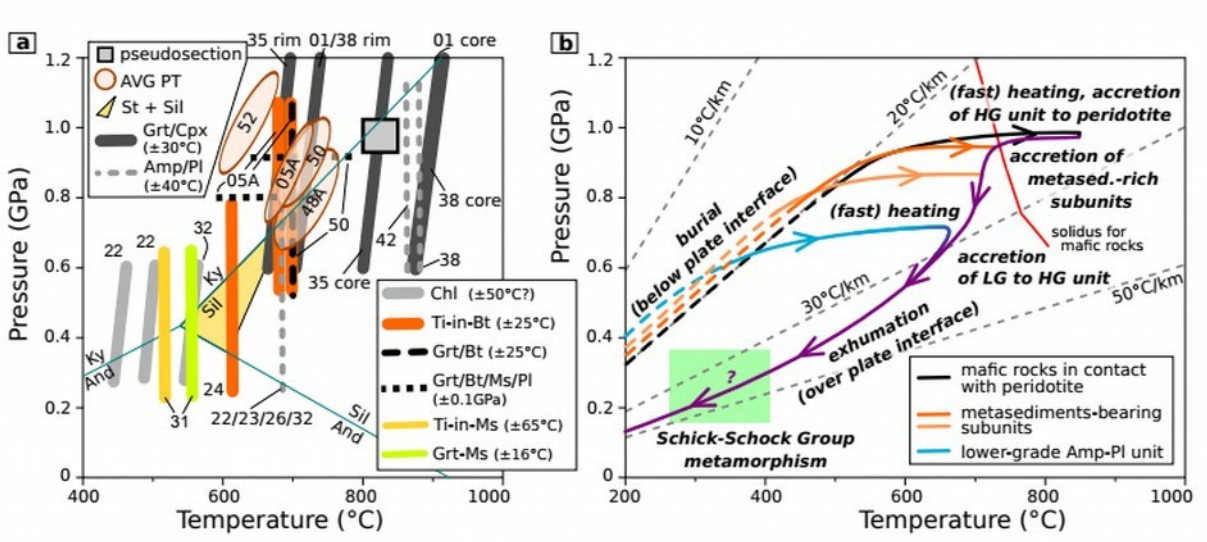

1177Figure 14: Compilation of thermobarometric estimates obtained in this study and inferred pressure-
1178temperature paths. (a) Thermobarometry results for mafic rocks (grey shades) and metasediments
1179(orange / green), reported as envelopes for AVG-PT, a box for results from the pseudosection (Fig.
118011), and sticks for chlorite thermometry, empirical pair equilibria and Ti solubility. Stability of
1181alumina-silicates from White et al. (2014a). (b) Pressure-temperature paths of subunits from the
1182metamorphic sole, leading to an apparent inverted metamorphic gradient. Rocks on top of the
1183metamorphic sole are subject to higher peak conditions than rocks structurally further from the contact
1184to the peridotite. All rocks all exhumed along the same path. The total number of subunits is unknown
1185and shown as three subunits with the higher-grade unit for readability. Note the different temperature
1186scales in (a) and (b).

1187

1188

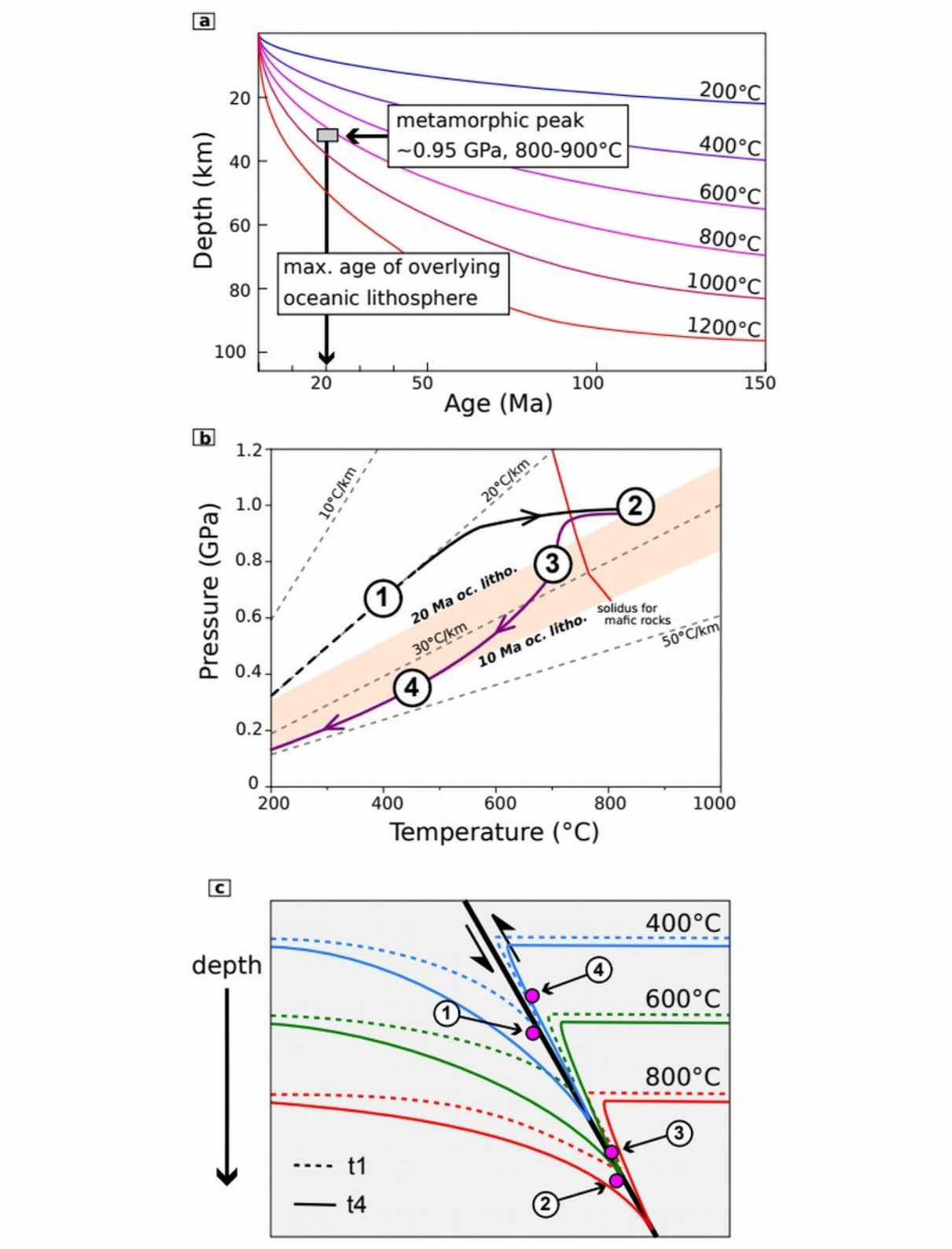

1189Figure 15: estimate of the evolution of the thermal structure of the lithosphere during metamorphic
1190sole creation. (a) Peak metamorphic conditions compared to temperature-depth profile of the oceanic

1191lithosphere as a function of age (from McKenzie et al., 2005). (b) Pressure-temperature evolution of 1192the high-grade unit, with four steps constraining the temperature evolution close to the interface, as 1193schematized in (c), where the plate boundary is sketched in black and isotherms are shown for step 1 1194(t1, dotted line) and step 4 (t4, solid line).

Table 1. Selected representative analyses of amphibole

Unit	High Grade Unit							
Sample	MA-14-34	MA-14-35	MA-14-38	MA-14-39	MA-14-40	MA-14-42	MA-12-22	MA-14-23
Analysis #	46	13	111	10	125	140	114	30
SiO_2	43,09	41,67	44,21	42,92	43,30	42,77	42,36	41,35
TiO_2	0,81	1,51	0,73	0,79	0,84	1,03	0,89	0,50
Al_2O_3	12,07	13,85	12,38	14,19	13,72	12,74	14,12	12,88
Cr_2O_3	0,05	0,01	0,10	0,04	0,56	0,04	0,08	0,09
FeO	15,19	14,74	13,47	12,49	9,60	15,32	15,85	19,63
MnO	0,24	0,06	0,14	0,07	0,40	0,21	0,28	0,43
MgO	10,70	10,51	11,82	11,77	12,85	10,52	10,37	8,68
CaO	11,58	11,84	11,67	11,86	12,27	11,61	11,21	10,89
Na_2O	1,84	1,92	1,73	1,49	1,76	1,91	2,02	1,79
K_2O	0,26	0,30	0,21	0,72	0,40	0,43	0,92	0,52
Σ	95,84	96,42	96,46	96,37	95,71	96,59	98,10	96,74
Ox.	23	23	23	23	23	23	23	23
Si	6,45	6,21	6,50	6,32	6,39	6,37	6,21	6,20
Aliv	1,55	1,79	1,50	1,68	1,61	1,63	1,79	1,80
Alvi	0,58	0,65	0,64	0,78	0,78	0,61	0,65	0,48
Ti	0,09	0,17	0,08	0,09	0,09	0,12	0,10	0,06
Cr	0,01	0,00	0,01	0,00	0,07	0,01	0,01	0,01
Fe^{3+}	0,48	0,40	0,47	0,42	0,12	0,44	0,67	1,08
Fe^{2+}	1,43	1,44	1,19	1,11	1,07	1,47	1,27	1,38
Mn	0,03	0,01	0,02	0,01	0,05	0,03	0,04	0,05
Mg	2,39	2,34	2,59	2,58	2,83	2,34	2,27	1,94
Ca	1,86	1,89	1,84	1,87	1,94	1,85	1,76	1,75
Na	0,53	0,56	0,49	0,43	0,50	0,55	0,57	0,52
K	0,05	0,06	0,04	0,14	0,08	0,08	0,17	0,10
Σ cat.	15,44	15,50	15,37	15,43	15,52	15,49	15,51	15,37
$[Na+K]^A$	0,44	0,50	0,37	0,43	0,52	0,49	0,51	0,37
XMg	0,63	0,62	0,69	0,70	0,73	0,61	0,64	0,58

Low Grade Unit					
MA-14-26		MA-14-28		MA-14-32	
88	78	61	56	127	125,1
42,58	52,68	43,36	50,68	43,61	53,47
0,50	0,07	0,54	0,16	0,47	0,12
12,70	3,20	11,48	5,42	12,81	3,25
0,05	0,00	0,03	0,04	0,01	0,00
16,84	11,73	17,81	13,06	16,29	11,90
0,36	0,24	0,26	0,25	0,27	0,34
10,65	16,53	10,33	14,86	10,70	15,97
10,91	11,70	11,01	12,07	11,17	11,65
2,03	0,66	2,00	0,90	2,03	0,74
0,37	0,11	0,26	0,12	0,38	0,14
97,01	96,90	97,07	97,55	97,74	97,59
23	23	23	23	23	23
6,27	7,51	6,42	7,28	6,38	7,60
1,73	0,49	1,58	0,72	1,62	0,40
0,48	0,05	0,42	0,20	0,59	0,15
0,06	0,01	0,06	0,02	0,05	0,01
0,01	0,00	0,00	0,00	0,00	0,00
1,03	0,65	0,92	0,50	0,78	0,45
1,04	0,75	1,28	1,07	1,22	0,96
0,05	0,03	0,03	0,03	0,03	0,04
2,34	3,52	2,28	3,18	2,33	3,39
1,72	1,79	1,75	1,86	1,75	1,77
0,58	0,18	0,57	0,25	0,58	0,20
0,07	0,02	0,05	0,02	0,07	0,03
15,37	14,99	15,37	15,13	15,40	15,00
0,37	0,02	0,37	0,13	0,40	0,03
0,69	0,82	0,64	0,75	0,66	0,78

Table 2. Selected representative analyses of clinopyroxene.

Unit	High Grade Unit								
Sample	MA-14-35			MA-14-38				MA-14-40	MA-14-42
Analysis #	23	30	41	80	84	100	102	111	135
SiO_2	47,70	50,37	47,82	48,35	50,39	51,40	51,30	51,12	50,09
TiO_2	0,50	0,37	0,62	0,55	0,27	0,07	0,13	0,25	0,34
Al_2O_3	6,92	3,96	6,80	6,61	4,08	3,54	3,94	4,11	4,43
Cr_2O_3	0,04	0,11	0,01	0,26	0,17	0,07	0,08	0,07	0,01
FeO	10,66	8,77	10,68	9,53	9,58	8,00	8,55	6,63	9,76
MnO	0,18	0,15	0,20	0,17	0,22	0,26	0,24	0,54	0,28
MgO	9,89	12,15	10,50	10,43	11,64	12,51	12,35	13,04	11,05
CaO	22,03	23,10	22,65	22,42	22,79	23,14	22,75	23,20	22,74
Na_2O	0,76	0,62	0,62	0,79	0,60	0,54	0,62	0,72	0,76
K_2O	0,02	0,00	0,00	0,00	0,01	0,01	0,00	0,01	0,01
Σ	98,69	99,61	99,91	99,12	99,76	99,54	99,95	99,68	99,47
Ox.	6	6	6	6	6	6	6	6	6
Si	1,83	1,90	1,81	1,84	1,90	1,93	1,92	1,91	1,90
Ti	0,01	0,01	0,02	0,02	0,01	0,00	0,00	0,01	0,01
Al_{tot}	0,31	0,18	0,30	0,30	0,18	0,16	0,17	0,18	0,20
Cr	0,00	0,00	0,00	0,01	0,00	0,00	0,00	0,00	0,00
Fe_{tot}	0,34	0,28	0,34	0,30	0,30	0,25	0,27	0,21	0,31
Mn	0,01	0,00	0,01	0,01	0,01	0,01	0,01	0,02	0,01
Mg	0,56	0,68	0,59	0,59	0,65	0,70	0,69	0,72	0,62
Ca	0,90	0,93	0,92	0,91	0,92	0,93	0,91	0,93	0,92
Na	0,06	0,05	0,05	0,06	0,04	0,04	0,05	0,05	0,06
K	0,00	0,00	0,00	0,00	0,00	0,00	0,00	0,00	0,00
Σ cat.	4,03	4,03	4,04	4,03	4,02	4,01	4,01	4,02	4,02
XMg	0,62	0,71	0,64	0,66	0,68	0,74	0,72	0,78	0,67

Table 3. Selected representative analyses of feldspar.

Mineral	Pl	Pl	Pl	Or	Or	Pl	Pl	Pl	Pl
Unit	High Grade Unit								
Sample	MA-14-34	MA-14-38		MA-14-39	MA-14-40	MA-14-42	MA-12-22	MA-14-23	MA-
Analysis #	60	89	73	12	109	134	104	20	41
SiO_2	68,87	47,26	45,71	64,39	64,74	47,21	61,96	62,61	60,42
TiO_2	0,00	0,00	0,00	0,00	0,00	0,00	0,00	0,00	0,00
Al_2O_3	19,89	33,52	34,93	18,50	18,53	33,10	24,14	23,34	24,83
Cr_2O_3	0,00	0,01	0,00	0,00	0,03	0,03	0,01	0,00	0,01
FeO	0,00	0,00	0,00	0,00	0,00	0,00	0,08	0,48	0,25
MnO	0,00	0,00	0,00	0,00	0,00	0,00	0,00	0,00	0,00
MgO	0,00	0,00	0,00	0,00	0,00	0,00	0,00	0,00	0,00
CaO	0,22	17,06	18,99	0,00	0,02	17,10	4,99	4,48	5,85
Na_2O	11,42	1,91	0,98	0,04	0,08	1,83	9,36	9,47	8,81
K_2O	0,04	0,00	0,01	16,23	15,61	0,02	0,14	0,07	0,11
Σ	100,43	99,75	100,61	99,15	99,01	99,29	100,67	100,46	100,29
Ox.	8	8	8	8	8	8	8	8	8
Si	2,99	2,17	2,09	2,99	3,00	2,18	2,74	2,77	2,69
Ti	0,00	0,00	0,00	0,00	0,00	0,00	0,00	0,00	0,00
Al_{tot}	1,02	1,81	1,89	1,01	1,01	1,80	1,26	1,22	1,30
Cr	0,00	0,00	0,00	0,00	0,00	0,00	0,00	0,00	0,00
Fe_{tot}	0,00	0,00	0,00	0,00	0,00	0,00	0,00	0,00	0,00
Mn	0,00	0,00	0,00	0,00	0,00	0,00	0,00	0,00	0,00
Mg	0,00	0,00	0,00	0,00	0,00	0,00	0,00	0,00	0,00
Ca	0,01	0,84	0,93	0,00	0,00	0,85	0,24	0,21	0,28
Na	0,96	0,17	0,09	0,00	0,01	0,16	0,80	0,81	0,76
K	0,00	0,00	0,00	0,96	0,92	0,00	0,01	0,00	0,01
Σ cat.	4,98	5,00	5,00	4,98	4,95	5,00	5,04	5,02	5,04
XAn	0,01	0,83	0,91	0,00	0,00	0,84	0,23	0,21	0,27
XAb	0,99	0,17	0,09	0,00	0,01	0,16	0,77	0,79	0,73
XOr	0,00	0,00	0,00	1,00	0,99	0,00	0,01	0,00	0,01

Or	Pl	Pl	Pl	Pl
Low Grade Unit				
14-24	MA-14-25	MA-14-26	MA-14-32	
49	56	86	147	133
63,57	63,95	63,14	62,90	68,37
0,00	0,00	0,00	0,00	0,00
18,19	23,14	22,71	24,04	20,58
0,01	0,00	0,00	0,00	0,02
0,18	0,17	0,31	0,27	0,31
0,00	0,00	0,00	0,00	0,00
0,00	0,00	0,00	0,00	0,00
0,00	4,16	3,92	5,00	0,74
0,20	10,13	10,24	9,33	11,82
16,85	0,09	0,05	0,07	0,05
99,00	101,63	100,36	101,60	101,89
8	8	8	8	8
2,98	2,79	2,79	2,75	2,95
0,00	0,00	0,00	0,00	0,00
1,01	1,19	1,18	1,24	1,04
0,00	0,00	0,00	0,00	0,00
0,00	0,00	0,00	0,00	0,00
0,00	0,00	0,00	0,00	0,00
0,00	0,00	0,00	0,00	0,00
0,00	0,19	0,19	0,23	0,03
0,02	0,86	0,88	0,79	0,99
1,01	0,00	0,00	0,00	0,00
5,02	5,04	5,05	5,02	5,02
0,00	0,18	0,17	0,23	0,03
0,02	0,81	0,82	0,77	0,96
0,98	0,00	0,00	0,00	0,00

Table 4. Selected representative analyses of micas

Min.	Bt	Ms	Ms	Bt	Bt	Ms	Bt	Ms
Loc.	Lower Grade Unit			Metasediment				
Smpl.	MA-14-24	MA-14-31		MA-14-05a			MA-14-50	
Anal.	37	8	9	16	36	34	74	80
SiO_2	36,14	46,20	45,59	34,62	35,43	48,14	37,04	45,83
TiO_2	1,94	0,26	0,24	3,03	2,53	0,00	2,36	0,27
Al_2O_3	17,80	31,83	33,46	18,60	19,07	34,52	18,20	33,87
Cr_2O_3	0,01	0,02	0,02	0,03	0,05	0,00	0,09	0,00
FeO	17,25	3,10	3,35	16,17	16,79	1,32	15,54	2,99
MnO	0,20	0,05	0,00	0,06	0,08	0,04	0,10	0,01
MgO	11,21	1,28	0,96	10,52	11,46	0,31	12,80	1,05
CaO	0,01	0,06	0,02	0,07	0,00	0,50	0,09	0,00
Na_2O	0,10	1,14	1,16	0,30	0,25	1,03	0,16	1,13
K_2O	9,67	9,75	9,71	8,99	9,35	9,20	8,89	9,58
Σ	94,33	93,68	94,50	92,41	95,01	95,07	95,27	94,74
Ox.	22	11	11	22	22	11	22	22
Si	5,51	3,16	3,09	5,36	5,34	3,18	5,51	3,09
Ti	0,22	0,01	0,01	0,35	0,29	0,00	0,26	0,01
Al_{tot}	3,20	2,56	2,67	3,39	3,39	2,69	3,19	2,69
Cr	0,00	0,00	0,00	0,00	0,01	0,00	0,01	0,00
Fe_{tot}	2,20	0,18	0,19	2,09	2,12	0,07	1,93	0,17
Mn	0,03	0,00	0,00	0,01	0,01	0,00	0,01	0,00
Mg	2,55	0,13	0,10	2,43	2,58	0,03	2,84	0,11
Ca	0,00	0,00	0,00	0,01	0,00	0,04	0,01	0,00
Na	0,03	0,15	0,15	0,09	0,07	0,13	0,05	0,15
K	1,88	0,85	0,84	1,78	1,80	0,78	1,69	0,82
Σ cat.	15,62	7,05	7,06	15,52	15,61	6,92	15,50	7,04
XMg	0,54	-		0,54	0,55	-	0,59	-
XPrl	-	0,00	0,01	-	-	0,06	-	0,03
XMs+XPg	-	0,84	0,91	-	-	0,82	-	0,91
Cel	-	0,16	0,08	-	-	0,13	-	0,06

Abbrevations after Whitney and Evans (2010).

Table 5. Selected representative analyses of epidote.

Unit	Low grade		Low grade		High grade		Low
Sample	MA-14-32		MA-14-22		MA-14-02		MA-
Analysis #	135	136	90	107	7	70	46
SiO_2	37,37	37,41	38,06	38,19	37,89	37,40	37,23
TiO_2	0,03	0,04	0,19	0,09	0,14	0,12	0,10
Al_2O_3	21,02	22,11	26,72	25,63	27,23	25,13	24,27
Cr_2O_3	0,03	0,00	0,10	0,19	0,01	0,02	0,00
FeO	14,87	14,20	8,62	10,62	7,37	10,37	11,13
MnO	0,12	0,21	0,13	0,32	0,25	0,49	0,37
MgO	0,00	0,00	0,00	0,00	0,12	0,03	0,02
CaO	23,24	23,39	23,48	23,07	23,17	22,56	22,76
Na_2O	0,02	0,00	0,04	0,01	0,00	0,05	0,02
K_2O	0,00	0,00	0,01	0,00	0,01	0,00	0,01
Σ	96,71	97,37	97,35	98,12	96,19	96,18	95,90
Ox.	12,5	12,5	12,5	12,5	12,5	12,5	12,5
Si	3,00	2,98	2,98	2,98	2,99	2,97	2,98
Ti	0,00	0,00	0,01	0,01	0,01	0,01	0,01
Al_{tot}	1,99	2,07	2,46	2,35	2,53	2,36	2,29
Cr	0,00	0,00	0,01	0,01	0,00	0,00	0,00
Fe3+	1,00	0,94	0,56	0,69	0,49	0,69	0,74
Mn	0,01	0,01	0,01	0,02	0,02	0,03	0,02
Mg	0,00	0,00	0,00	0,00	0,01	0,00	0,00
Ca	2,00	2,00	1,97	1,93	1,96	1,92	1,95
Na	0,00	0,00	0,01	0,00	0,00	0,01	0,00
K	0,00	0,00	0,00	0,00	0,00	0,00	0,00
Σ cat.	8,00	8,01	8,00	7,99	8,00	8,00	8,00

grade	Low grade		High grade		High grade	
14-24	MA-14-28		MA-14-35		MA-14-38	
47	58	59	36	39	54	57
36,66	37,48	36,99	39,17	39,09	38,38	38,69
0,05	0,09	0,12	0,02	0,05	0,30	0,00
22,53	22,98	21,58	28,35	28,27	24,92	28,19
0,03	0,02	0,01	0,00	0,01	0,00	0,01
13,19	12,45	14,47	6,23	6,31	9,75	6,22
0,42	0,10	0,08	0,10	0,12	0,13	0,23
0,00	0,00	0,00	0,02	0,04	0,13	0,04
22,59	23,11	22,82	24,26	23,73	23,40	23,91
0,00	0,00	0,00	0,01	0,00	0,00	0,00
0,03	0,00	0,01	0,02	0,02	0,00	0,02
95,49	96,23	96,07	98,18	97,65	97,03	97,32
12,5	12,5	12,5	12,5	12,5	12,5	12,5
2,97	3,00	2,98	3,02	3,02	3,02	3,00
0,00	0,01	0,01	0,00	0,00	0,02	0,00
2,15	2,17	2,05	2,57	2,57	2,31	2,58
0,00	0,00	0,00	0,00	0,00	0,00	0,00
0,89	0,83	0,98	0,40	0,41	0,64	0,40
0,03	0,01	0,01	0,01	0,01	0,01	0,02
0,00	1,98	1,97	0,00	0,00	0,02	0,01
1,96	0,00	0,00	2,00	1,96	1,97	1,99
0,00	0,00	0,00	0,00	0,00	0,00	0,00
0,00	0,00	0,00	0,00	0,00	0,00	0,00
8,01	7,99	8,00	8,00	7,99	7,99	8,00

High grade				High grade		
MA-14-40				MA-14-37		
120	121	122	51	3	9	11
38,95	39,21	38,99	37,81	37,47	38,23	38,33
0,05	0,02	0,17	0,28	0,09	0,25	0,01
29,54	31,67	28,68	22,01	21,44	25,30	27,73
0,00	0,03	0,25	0,02	-0,01	0,04	-0,01
3,60	1,56	4,64	12,97	13,52	9,82	6,59
0,18	0,05	0,19	0,18	0,16	0,09	0,16
0,08	0,00	0,09	0,02	-0,03	0,07	0,03
24,08	24,57	23,96	23,51	22,70	23,75	23,60
0,00	0,05	0,03	0,01	0,01	0,04	0,02
0,00	0,02	0,02	0,01	0,00	0,02	-0,02
96,49	97,19	97,02	96,82	95,34	97,62	96,44
12,5	12,5	12,5	12,5	12,5	12,5	12,5
3,03	3,01	3,03	3,02	3,03	2,99	3,01
0,00	0,00	0,01	0,02	0,01	0,01	0,00
2,71	2,86	2,62	2,07	2,05	2,34	2,56
0,00	0,00	0,02	0,00	0,00	0,00	0,00
0,23	0,10	0,30	0,87	0,92	0,64	0,43
0,01	0,00	0,01	0,01	0,01	0,01	0,01
0,01	0,00	0,01	0,00	0,00	0,01	0,00
2,01	2,02	1,99	2,01	1,97	1,99	1,98
0,00	0,01	0,01	0,00	0,00	0,01	0,00
0,00	0,00	0,00	0,00	0,00	0,00	0,00
8,00	8,01	8,00	8,00	7,98	8,00	8,00

Table 6. Selected representative analyses of garnet.

Unit	Mafic rocks, high grade unit							
Sample	MA-14-39		MA-14-35		MA-14-38		MA-14-34	MA-14-37
Analysis #	4	5	5	46	92	3	78	31
SiO_2	39,39	38,97	38,64	38,09	38,77	38,93	38,64	37,70
TiO_2	0,00	0,00	0,04	0,07	0,02	0,03	0,01	0,06
Al_2O_3	21,65	21,59	20,66	20,65	21,04	21,76	21,01	20,92
Cr_2O_3	0,03	0,05	0,03	0,00	0,02	0,08	0,00	-0,02
FeO	23,79	23,60	22,76	23,75	21,85	20,85	24,48	26,96
MnO	1,08	1,00	1,24	1,68	2,63	1,35	2,40	2,90
MgO	7,69	7,66	5,49	4,69	4,74	7,15	5,17	3,35
CaO	6,72	6,72	10,97	10,83	10,86	10,44	7,55	7,56
Na_2O	0,00	0,00	0,03	0,00	0,00	0,00	-0,02	-0,01
K_2O	0,01	0,01	0,02	0,00	0,00	0,00	-0,01	0,02
Σ	100,36	99,60	99,88	99,75	99,93	100,59	99,24	99,46
Ox.	12	12	12	12	12	12	12	12
Si	3,02	3,01	3,01	2,99	3,02	2,98	3,04	3,00
Ti	0,00	0,00	0,00	0,00	0,00	0,00	0,00	0,00
Al_{tot}	1,96	1,96	1,90	1,91	1,93	1,96	1,95	1,97
Cr	0,00	0,00	0,00	0,00	0,00	0,00	0,00	0,00
Fe_{tot}	1,52	1,52	1,48	1,56	1,42	1,33	1,61	1,80
Mn	0,07	0,07	0,08	0,11	0,17	0,09	0,16	0,20
Mg	0,88	0,88	0,64	0,55	0,55	0,81	0,61	0,40
Ca	0,55	0,56	0,92	0,91	0,91	0,86	0,64	0,65
Na	0,00	0,00	0,00	0,00	0,00	0,00	0,00	0,00
K	0,00	0,00	0,00	0,00	0,00	0,00	0,00	0,00
Σ cat.	8,00	8,01	8,04	8,04	8,01	8,04	7,99	8,01

Table 6. Selected representative analyses of minor phases.

Mineral	St	Scp	Mrg-rich Phg	Mrg-rich Phg	Mrg-rich Phg	Pmp	Chl
Unit	Metasediment			High grade		High grade	High
Sample	MA-14-14	MA-14-12		MA-14-02		MA-14-34	MA-1
Analysis #	27	13	9	10	72	64	84
SiO_2	27,04	45,17	41,86	36,14	44,38	36,51	26,26
TiO_2	0,65	0,04	0,09	0,01	0,32	0,04	0,04
Al_2O_3	53,76	24,84	42,50	45,69	39,69	21,67	20,85
Cr_2O_3	0,00	0,00	0,00	0,01	0,00	0,03	0,03
FeO	12,84	0,17	0,86	1,02	1,12	8,91	22,90
MnO	0,18	0,00	0,02	0,00	0,00	0,13	0,37
MgO	1,78	0,00	0,18	0,38	0,14	2,27	17,49
CaO	0,00	16,54	3,06	7,02	1,16	22,64	0,03
Na_2O	0,00	4,04	6,43	4,18	6,43	0,02	0,00
K_2O	0,00	0,00	0,73	0,42	1,61	0,00	0,04
Σ	96,25	90,80	95,74	94,86	94,85	92,22	88,02
Ox.	22	24	11	11	11	12	14
Si	3,63	6,94	2,71	2,39	2,89	2,99	2,72
Ti	0,07	0,00	0,00	0,00	0,02	0,00	0,00
Al_{tot}	8,52	4,50	3,24	3,56	3,04	2,09	2,55
Cr	0,00	0,00	0,00	0,00	0,00	0,00	0,00
Fe_{tot}	1,44	0,02	0,05	0,06	0,06	0,61	1,98
Mn	0,02	0,00	0,00	0,00	0,00	0,01	0,03
Mg	0,36	0,00	0,02	0,04	0,01	0,28	2,70
Ca	0,00	2,72	0,21	0,50	0,08	1,98	0,00
Na	0,00	1,20	0,81	0,54	0,81	0,00	0,00
K	0,00	0,00	0,06	0,04	0,13	0,00	0,00
Σ cat.	14,04	15,40	7,10	7,11	7,05	7,97	10,00
XMg	0,20	-	0,27	0,40	0,19	0,31	0,58

Chl grade
14-22
85
26,33
0,06
20,44
0,02
23,18
0,43
17,50
0,06
0,03
0,02
88,07
14
2,73
0,00
2,50
0,00
2,01
0,04
2,71
0,01
0,01
0,00
10,01
0,57